PROTOTYPE L-BAND SYNTHETIC APERTURE RADAR

ON LOW-ALTITUDE / NEAR-GROUND PLATFORMS

A Dissertation

Submitted to the Faculty

of

Purdue University

by

Man Chung Chim

In Partial Fulfillment of the

Requirements for the Degree

of

Doctor of Philosophy

December 2018

Purdue University

West Lafayette, Indiana

THE PURDUE UNIVERSITY GRADUATE SCHOOL
STATEMENT OF APPROVAL

Dr. Daniele Perissin, Chair

    Lyles School of Civil Engineering

Dr. Ayman F. Habib

    Lyles School of Civil Engineering

Dr. Mark R. Bell

    Department of Electrical and Computer Engineering

Dr. Michael Zoltowski

    Department of Electrical and Computer Engineering

Approved by:

    Dr. Dulcy M. Abraham

        Head of the Graduate Program

ACKNOWLEDGMENTS

This research could not be made possibe with the support from different parties, and the author feels very thankful to each individuals and groups who has provided inputs and advices to the research work. In particular, the author would like to thank you for the support from his family over the years, during days where things are breaking down, it was those cheerful words that keep the work on going. The author would also like to thank you the colleagues working at the research laboratories on 4th floor of Hampton Hall of Civil Engineering for the inspirational discussions. The advices from the supervising committees are very much appreciated. And lastly, great thanks to the colleagues at Zendar Inc. who have been providing a nice research environment towards the final stage of the research work.

PREFACE

This document serve as a research conclusion report for fulfilling graduation requirement of Doctor of Philosophy in Lyles School of Civil Engineering, Purdue University. Algorithms and Hardware implementation are discussed, and research results are included. The documents has covered from the basic proof-of-concept to implementation, and the author has made his best effort in keeping the theory and implementation accurate. However, since Synthetic Aperture Radar systems are very taylored to specific use case, if anything is unclear or cannot be generalized to a particular research case, please feel free to discuss with the author.

TABLE OF CONTENTS

LIST OF FIGURES

ABSTRACT

Chim, Man Chung PhD, Purdue University, December 2018. Prototype L-band Synthetic Aperture Radar on Low-altitude / Near-ground platforms. Major Professor: Daniele Perissin.

Synthetic Aperture Radar (SAR) is a technique to synthesize a large antenna array using the motion of a small antenna. When it comes to remote sensing, mapping, and change detection, SAR has been shown to be a good candidate by its ability to penetrate moisture and vegetation, and the avilibility of phase information for precise interferometric measurements [1] [13].

This study was motivated by the fact that satellite and high-altitude SAR has limited data availability in terms of temporal resolution and the cost of every measurement. It is believed that SAR systems mounted on smaller UAV or ground vehicles could provide a much better coverage of the target in time, and in different geometry.

We proposed a L-band SAR system based on Software-Defined Radio to be mounted on automotive platform. Novel motion estimation and compensation, as well as autofocusing techniques were developed to aid the SAR signal processing under much more demanding environment - the instability of radar platforms. It is expected this research development could bring down the cost of SAR being used as a remote sensing solution, and allow SAR system to be mounted on much smaller platforms by overcoming the instability of the track using novel signal processing methods, and eventually making SAR measurement available in places and times that was previously impossible.

1. RESEARCH OUTLINE

1.1 Motivation

When talking about remote sensing, there are mainly 3 distinct techniques, namely camera, Lidar, and Radar [5]. Camera has caught great attention among developers recently thanks to multiple deep learning framework with pre-trained networks made available, and the well developed opencv library. Lidar, on the other hand, targets professional users given the high cost of operation. Even though these are well established techniques, there are some disadvantages in each of them. For example, the camera being a passive sensor, lacks the ability to measure range accuratly using the time-of-flight technique. Lidar relys on a pulsed measurement which limited its range due to limited peak power handling ability of the diode. Radars on the other hand, is able to measure objects to a far range with low peak power using pulse compression. Using the doppler information, Radars can also measure the range velocity which no other sensors is capable of. The major problem in Radar is the low spacial resolution. Range resolution of a radar is limited by the bandwidth of signal its transceiver chain can handle, while the Azimuth resolution of a radar is limited by the ratio of center wavelength to size of antenna [21]. Consider a mono-static radar with antenna size approximately 1 meter and operating frequency of 1GHz, the beamwidth is at a laughable 17 degrees compared less than 0.01 degrees in most Lidar and camera systems.

Another feature which is achievable by Radar but not Lidar and camera is the ability to see through moisture, and vegetation in some frequencies. This feature is particularly useful considering the use case of precipitation detection in weather radar, target detection on vegetated ground in airborne surveillance radar, and collision avoidance for automotive driving in fog, snow, or rain.

Obviously, Radar is an essential component in a lot of sensor fusion solution given the above arguements, however, not at its current state. There was a hugh advancement in Radar signal processing following the invention of Synthetic Aperture technique. Simply speaking, synthetic aperture is a way to synthesize a large antenna by moving a small antenna incrementally when transceiving successive pulses, or chirps. Alternatively, one can think of a synthetic aperture as a huge phased array, while there is a separate analog-digital-converter (ADC) behind each antenna element instead of a phase-shifter in most phase array systems. This technique greatly enhance the azimuth resolution of the resultant Radar image (Here we assume a monostatic Radar moving on a linear track). Hence solved the major problem in Radar remote sensing, the low spatial resolution. [12] [17] [18] [27]

By utilizing lower frequency bands, the electromagnetic (EM) wave in general has better penetrating power. This can be particularly useful when monitoring structures where there are vegetation and/or other small and unstable objects along the line-of-sight (LOS) between Radar antenna and the target of interest.

The above solutions are well known theoretically, but hard to solve practically in the engineering sense. Radar systems are not commonly available off-the-shelf, there are a few companies manufacturing Ku-band ground based SAR systems that operates on a linear rail, which does badly in terms of penetrating vegetation. If the requirement is a Radar system that is designed for synthetic aperture on a custom mobile platform (ground vehicle or small aerial platform), the answer is simply none. One can say, as long as the raw signal or the IF signal is available, SAR can be separated into a real aperture radar system plus some signal processing that synthesize the aperture, but in reality a lot of the synthetic aperture parameters are tightly bonded to the hardware specifications, for example, the beamwidth of antenna. Hence a custom designed L-band SAR system is required.

Even more, building a SAR system on small ground-based or low-altitude platform is much more challenging than space-borne or high-altitude in terms of trajectory control. (Here ground-based defines the geometry and stability of the radar mount, and

does not mean the radar is operating on a linear rail as some company has marketed with similar wordings.) In space, even if the trajectory may not be well know, it is approximately linear over the synthetic aperture length, hence a standard focusing kernel in Range Doppler algorithm (RDA) or Omega-K algorithm (ωKA) can be used to generate 'some sort' of imagery. Similar applies to high-altitude aircraft where there is little turbulence, whenever the trajectory is stable or approximately linear, the SAR problem is deterministic and straight forward. This assumption is totally broken when we bring the system to low-altitude or automotive. The trajectory is highly non-linear in these platforms, that if we rely on the linear track approximation, the image is often highly defocused. As a result, the problem is usually not deterministic, as we can see in many autofocusing algorithm that employs an iterative approach. In some cases, not even the stock autofocusing techniques could improve the defocused image due to the difference in geometry caused by much lower elevation angle.

1.2 Contributions

Given the above arguments, the author has done a series of research work to study the behavior of SAR imaging on highly unstable ground-based platforms.

A first prototype SAR platform was built to evaluate the performance and potential problems of a L-band ground-based SAR. Then a second prototype was built to bring in MIMO capability, which was essential for the new autofocusing algorithm being developed. Afterward, work has been done in modifying existing autofocusing algorithms, as well as developing Novel methods to estimate the radar motion. Contributions have been made in the following areas:

1.2.1 Prototype SAR system based on Vector Network Analyzer

The first prototype was a testing platform built from modifying the GBSAR systems manufactured by LiSALAB, which was based on a Vector Network Analyser [4].

The system was taken off from the linear rail, and connected to a GNSS/INS system by Novatel, then installed on a pick-up truck for evaluating the performance of L-band mobile SAR. The data collected was compressed using the standard Range-Doppler Algorithm with minimal motion compensation techniques applied. The main objective for this prototype was to evaluate the feasibility, performance, and imaging quality of L-band SAR systems under the specific near-ground geometry, and how motion error would affect the sharpness of the image. Details and results are shown in Chapter 4.

1.2.2   Prototype Radar system based on Software Defined Radio

The author realized the capability of using Software-Defined Radio in Radar systems which has emerged relatively recently thanks to the advancement in processing power of general-purpose processors and sampling rate of ADCs, and has built a second Radar prototype based on the Universal Software Radio Peripheral (USRP) by Ettus Research, operating at L-band (1-2GHz). On top of that, a signal processing chain and chirp profile was designed for this Radar prototype to extend its chirp bandwidth from 56MHz to hundreds of MHz (limited by the handling of antenna). The USRP, which is capable of operating in 2x2 MIMO mode, has one TX and two RX activated in the prototype, which is exploited by the newly developed motion estimation and autofocusing algorithms. Hardware prototype is discussed in chapter 5.

The major advancement from the second Radar prototype was to extend the bistatic antenna configuration in first prototype to 1Tx 2Rx configuration for accommodating the autofocusing algorithm requirements. And the major challenges was to redesign the signal processing chain such to enable the USRP to scan a wide bandwidth.

1.2.3 Modified Phase Gradient Algorithm

Majority of the work in autofocus has been evaluating and improving the Phase Gradient Autofocus Algorithm (PGA) given its robustness [22]. The original PGA estimates the phase gradient by using the maximum-likelihood estimator operated along range direction for each pair of chirp. The result is similar to taking an average of phase gradient for each range bins with uniform weighting. This method makes much sense in high-altitude SAR systems given that the range from radar to scene center is much larger than the size of the scene, hence the vibration of the platform can the thought to have very similar magnitude and direction of effect to the phase error in each of the range bins. This is not true for ground based systems where the region of interest (ROI) often starts from range zero. Theoretical development has been done to modify the existing PGA with some motion modeling, and the newly developed algorithm has been tested with both simulated data and real radar return signal. More of this is discussed in chapter 6.

1.2.4 MPGA - A Novel Motion Estimation and Compensation Method

A novel algorithm called MIMO Phase Gradient Algorithm (MPGA) has been developed. The naming comes from the idea that Phase Gradient Algorithm made use of iterative method operating on a pre-focused image to estimate the phase error, while MPGA uses the doppler information from MIMO return signals to compute the motion in a more deterministic way. The algorithm is capable of solving the relative motion between each dominant targets and the Radar. When assuming all targets are stationary in the scene, it is been shown that this algorithm can focus the SAR image without any track or timing information. In SAR systems where GPS/IMU is available, this algorithm can be relaxed to solve for more than one velocities to identify and focus moving targets together with stationary targets. The algorithm has been tested with simulated as well as real radar return signal. Ideally given there are enough contrast in the scene and/or a number of corner-reflector-like targets, a

SAR system equipped with this algorithm can focus on its own without messing with the timing and positioning problem. Details of the algorithm is outlined in chapter 7.

2. INTRODUCTION

2.1 Radar Basics

2.1.1 Range Pulse Compression [21]

A Radar is a range detection system that consist of a signal generator, antenna, receiver, and processor (correlator). The processor being the core of the system, enables the Radar to compute the time-of-flight of the received signal, hence the range to targets along the signal path.

Consider the simplest Radar model where a rectangular pulse is being sent by a mono-static Radar in a noiseless environment, and assume there is a single target at range R_0 from the antenna, the return pulse will be detected at a delay of τ:

$$\tau = \frac{2R_0}{c} \tag{2.1}$$

where c is the speed of light in air, approximately $299792458 ms^{-1}$ (in vacuum).

Maximum range depends on the length of the correlator, i.e. the length of register in the processor. Assume minimum detectable SNR of the radar receiver is not a limiting factor, the longer the register, the larger the maximum range.

Range resolution depends on how narrow the pulse is, if the pulse has length of t_0, the resolution is defined to be the minimum detectable separation of the 2 return pulses, which is t_0. When measured in meters, it is:

$$\delta R = \frac{t_0 c}{2} \tag{2.2}$$

While theoretically correct, this is not a clever utilization of the transceiver hardware in the sense that a very high peak power is required when sending a short pulse,

and there is a long quiet time that brings down the average power requirement. The short peak power is not well handled by most electronic components. The pulse compression technique solves this problem.

The main requirement here is having a short pulse in the time axis, by utilizing the Fourier transform relation, we know a delta in time is a wide spread in frequency. Hence, one can transmit a signal of incrementally increasing frequency, collect the returned signal which is in frequency axis, and perform a Fourier transform to obtain an equivalent short pulse in time.

There are many frequency modulation schemes and each yields a different ambiguity function, for simplicity we take a non-baseband Linear Frequency Modulation (LFM) signal as an example. Non-baseband LFM signal has the form:

$$s(t) = A(t)exp(j2\pi(f_0 + \alpha t)t) \tag{2.3}$$

where $A(t)$ is the amplitude envelop, usually constant, or being a Taylor window to reduce sidelobes; f_0 is the starting frequency; α is the chirp rate; t is the fast time.

Consider the same situation as above, a single target in noiseless environment, and we perform match filtering of the received signal, the result will be a sinc function centered at the target delay, with some encoded phase:

$$s_{MF}(t) = \int_{-T/2}^{T/2} s(t)s^*(-t+\tau)dt \tag{2.4}$$

$$= Texp(-j2\pi f_c(t-\tau)) \cdot sinc(\alpha T(t-\tau)) \tag{2.5}$$

where f_c is the center frequency; τ is the round trip delay to the target; T is the chirp duration.

Range resolution is usually defined by the Full Width Half Maximum (FWHM), i.e. -3dB width of the sinc envelop, which is:

$$\delta R = \frac{c}{2} \frac{0.886}{\alpha T} \tag{2.6}$$

$$\approx \frac{c}{2B} \tag{2.7}$$

Equation (2.2) and (2.7) can be shown equivalent by the time-frequency conversion of:

$$t_0 = \frac{1}{B} \tag{2.8}$$

Hence the wider the bandwidth, the higher the range resolution, with the energy being spread equally to different frequencies at different fast time instance.

2.1.2   The Ambiguity Function [23] [40]

Radar measurement is ambiguous because of undersampling, range-doppler coupling, and presence of sidelobes. For instance, if there is a target moving along range direction of a SAR system that is transmitting LFM chirp, the resultant imagery will show a perfectly focused image but with the target shifted to a totally different azimuth position. This can cause great headache as one cannot tell the image is problematic from the focusing quality. The reason behind this artifact is that the moving target has a doppler component which is not compensated in the range compression stage.

The ambiguity function provides some insight into designing a proper Radar waveform (or chirp profile) by computing analytically the auto-correlation of the waveform in time-frequency space.

Consider the transmitted signal being $s(t)$, the (asymmetric) ambiguity function $\Phi(\tau, \nu)$ is defined to be:

$$\Phi(\tau, \nu) = \int_{-\infty}^{\infty} s(t)s^*(t - \tau) \cdot exp(j2\pi\nu t)dt \tag{2.9}$$

In the case of LFM waveform in (2.3), assume $A(t) = 1_{[-\frac{T}{2}, \frac{T}{2}]}(t)$, the ambiguity function yields:

$$|\Phi(\tau, \nu)| = (T - |\tau|) \cdot sinc((T - |\tau|)(\nu + k\tau)) \qquad (2.10)$$

2.1.3   The Radar Equation

The Radar equation provides help in computing the required power and SNR for the system to work at certain range. For monostatic Radar, the equation is given as [21]:

$$P_{rx} = \frac{P_{tx}G^2\sigma\lambda^2}{(4\pi)^3 R^4} \qquad (2.11)$$

where P_r is the power of signal received; P_s is the power of signal transmitted; G is the gain of antennas; λ is the center wavelength; R is the one-way range from antenna to target.

The receiver usually specify a minimum detectable signal to noise ratio (SNR), with that, we can compute the transmit power required to attain certain range.

One must note that this equation is defined for a real aperture radar, and cannot be applied directly to synthetic aperture radar. Synthetic aperture radar systems usually have much higher detecting power due to the large aperture being synthesized. i.e. Even if a target is not visible in the range profile, it can pop up after azimuth compression.

One way to approximately convert the equation between real and synthetic aperture is to find the effective gain G using the synthetic aperture length.

2.2   Stretch Processing

Stretch processing is a way of signal processing in the transceiver chain [35] [36]. Compared to conventional matched filtering techniques, stretch processing do not

store the the received signal in a register then correlate it with a copy of the transmitted signal. Instead, the received signal is mixed (multiplied) with the transmitted signal instantaneously, shown in figure 2.1.
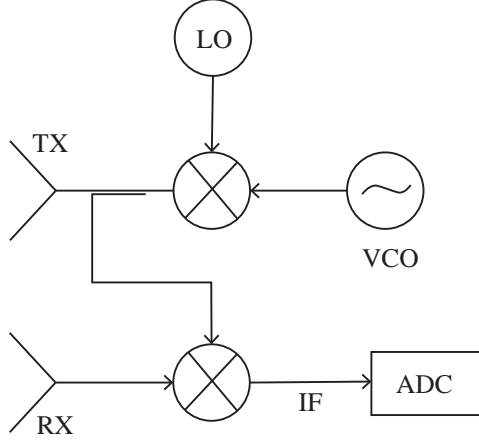
Figure 2.1. Simplified hardware schematic for Stretch Processing

VCO is the voltage controlled oscillator which generates the baseband chirp, LO is the local oscillator that generates the carrier frequency. The signal received is immediately mixed (multiplied) with a copy of the transmitted signal, and the intermediate frequency (IF) signal yielded is inputted into the analog-digital converter (ADC).

2.2.1   The Signal Model

Consider a LFM transmitted signal in equation (2.3), where $A(t) = rect(t/T)$, the received signal has the form [20]:

$$s_{rx}(t) = rect(\frac{t-\tau}{T}) \cdot exp(j2\pi(f_0 + \alpha(t-\tau))(t-\tau)) \qquad (2.12)$$

where τ is the delay from target.

The intermediate frequency (IF) signal is obtained by mixing (2.3) with (2.12):

$$s_{IF}(t) = s_{rx}(t) \cdot s_{tx}^*(t) \tag{2.13}$$

$$= exp(j2\pi(f_0 + \alpha t)t) \cdot exp(j2\pi(f_0 + \alpha(t - \tau))(t - \tau)) \tag{2.14}$$

$$= 1_{[-T/2+\tau, T/2]}(t) \cdot exp(j2\pi f_0\tau) \cdot exp(-j2\pi\alpha\tau^2) \cdot exp(j2\pi\alpha\tau t) \tag{2.15}$$

The first phase term in equation (2.15) has the round trip delay time τ encoded in the fast varying phase at the carrier frequency. The second phase term is the Residual Video Phase (RVP) which is a function of τ. The third phase term is the range-azimuth coupling.

Taking Fourier transform along the fast time axis t, we can obtain the signal model in frequency axis f, where the IF frequency is directly proportional to the round trip delay time from Radar antenna to the target.

$$s_{IF}(t) = \int_{-\infty}^{\infty} 1_{-T/2+\tau, T/2}(t) \cdot exp(j2\pi f_0\tau) \cdot exp(-j2\pi\alpha\tau^2) \cdot exp(j2\pi\alpha\tau t) \cdot exp(-j2\pi ft)dt \tag{2.16}$$

$$= exp(j2\pi f_0\tau) \cdot exp(-j2\pi\alpha\tau^2) \cdot \int_{-T/2+\tau}^{T/2} exp(j2\pi\alpha\tau t) \cdot exp(-j2\pi ft)dt \tag{2.17}$$

$$= exp(j2\pi f_0\tau) \cdot exp(-j2\pi\alpha\tau^2) \cdot \int_{-T/2+\tau}^{T/2} exp(j2\pi(\alpha\tau - f)t)dt \tag{2.18}$$

$$= exp(j2\pi f_0\tau) \cdot exp(-j2\pi\alpha\tau^2) \cdot \frac{1}{j2\pi(\alpha\tau - f)} \cdot (e^{j2\pi(\alpha\tau-f)(T/2)} - e^{-j2\pi(\alpha\tau-f)(T/2)}e^{j2\pi(\alpha\tau-f)\tau}) \tag{2.19}$$

$$\approx exp(j2\pi f_0\tau) \cdot exp(-j2\pi\alpha\tau^2) \cdot \frac{1}{j2\pi(\alpha\tau - f)} \cdot (e^{j2\pi(\alpha\tau-f)(T/2)} - e^{-j2\pi(\alpha\tau-f)(T/2)} \tag{2.20}$$

$$= exp(j2\pi f_0\tau) \cdot exp(-j2\pi\alpha\tau^2) \cdot sinc(T(\alpha\tau - f)) \cdot T \tag{2.21}$$

$$= exp(j2\pi f_0\tau) \cdot exp(-j2\pi\alpha\tau^2) \cdot sinc(\alpha T(\tau - f/\alpha)) \cdot T \tag{2.22}$$

Equation (2.22) is the signal model we use for the rest of the discussion. The first 2 phase terms remained as they are fast-time-independent. The last phase term is

linear in fast time, hence 'compressed' into a sinc (or delta) function after the Fourier transform. The width of sinc is determined by αT, which is the bandwidth of the signal. The position of the sinc is determined by the round trip delay time τ. The translation between frequency axis f and time delay axis τ is given as:

$$\tau = \frac{f}{\alpha} \tag{2.23}$$

Assumptions taken by this signal model are:

- LFM signal is being transmitted.

- The sampling along fast time is uniform.

- There is no relative motion between target and radar within a chirp.

- No non-linearity is being introduced by the RF components.

2.2.2   Step Frequency Radar

This technique is also used in the design of step frequency Radars, where a signal of constant frequency is being sent one after another, which acts as sampling along the frequency axis, and the chirp compression is done by putting each of these frequency samples in place followed by a Fourier transform along the frequency axis. This way, assuming there is no moving object over the duration of measurement, the Radar can scan the frequencies and not having to worry about the bandwidth of the ADC, as long as both signal going into the receive mixer shares the same local oscillator (LO). More of this is discussed in chapter 5 section 4.

2.3   Synthetic Aperture Radar (SAR)

The concept of Synthetic Aperture Radar was proposed by Carl Wiley in 1951 while he was working at Lockheed Martin legacy company Goodyear Aircraft Company. It works by collecting pulses at multiple positions along the flight path of the

Radar system, saving the return signal in memory, and perform pulse compression (similar to range pulse compression) along the azimuth direction [21].

Unlike real aperture Radar systems, which requires a huge physical antenna to create a narrow beam in order to achieve fine azimuth resolution, synthetic aperture Radar systems utilize small antenna with wide beamwidth. The azimuth resolution is inversely proportional to the beamwidth of the antenna. This can be understood as a wider beam being capable of illuminating the target for a longer duration, hence a longer synthetic aperture could be formed. A long synthetic aperture translates to wider azimuth bandwidth, and a finer azimuth resolution.

The azimuth pulse compression can be performed in various ways, in frequency domain or time domain. While these algorithms varies largely between each other, the goal behind was just to figure out a better approximation of the ideal imaging and balancing between computation power required versus error induced in the imagery. Some of the well known SAR focusing algorithms are discussed in chapter 3.

While the basic SAR theory is very simple and deterministic, in fact most of the focusing algorithm is just a constant kernel computed from the constant velocity of the Radar platform, converting the theory to practical/production system is pretty hard. One major issue is the uncertainty of the track of Radar. The maximum tolerable error of the relative Radar track is often a small fraction (less than one-tenth) of the carrier wavelength in order to get a reasonably focused target. That is less than 3cm for L-band, less than 3mm for X-band, and less than 0.4mm for W-band! (We define relative Radar track to be the track that can have arbitrary constant offset, which only affect the position of the target but not its sharpness.) In open area or aerial platform, 3cm or 3mm relative accuracy may be still achievable by a good GNSS/INS system, however that is not always true especially for ground vehicles, lower-altitude crafts, or higher frequency systems. One way to solve the positioning error is to employ autofocusing algorithms, which will be discussed in chapter 6. Most autofocusing algorithms make use of the phase information from the returned signal (with Maximum Entropy be an exception) to estimate which part of

that phase is the actual signal from target, which part is from other error sources. Removing the error phase vector improves the image focusing quality.

Most autofocusing algorithms are iterative in nature, rendering them useless in most real-time SAR imaging systems. Therefore apart from autofocusing, the author has proposed an novel alternative method named MPGA to solve the track error. MPGA utilize MIMO transceiver to solve for the position of the Radar. Compared to other GNSS/INS positioning solutions which have a different update rate than the Radar pulse repetition frequency, different positions on the system frame, and different timing by isolated clocks on each sensors, the MPGA is a beautiful solution as the position being solved is exactly per chirp at the antenna itself. MPGA is discussed in chapter 7.

2.3.1 Azimuth Pulse Compression

SAR azimuth compression works by collecting a series of return signal at discrete positions along the flight path. Consider the simpliest geometry shown in figure 2.2, where a monostatic Radar is flying linearly along azimuth direction at constant velocity and looking at Range direction, a configuration we called broadside and stripmap, the instantaneous range between Radar antenna and the target is denoted by $R(x)$. Since the flight path is linear and uniform, $R(x)$ is just [21]:

$$R(x) = \sqrt{R_0^2 + x^2} \tag{2.24}$$

$$\approx R_0 + \frac{x^2}{2R_0} - \frac{x^4}{8R_0} + \cdots \tag{2.25}$$

From the direct relation between range and round-trip delay time in (2.1) and the signal model in (2.22), the instantaneous range $R(x)$ is encoded in both the phase and amplitude of the signal. Here we removed the RVP term after range compression.

$$s_{IF}(f, x) = exp(j\frac{4\pi}{\lambda}R(x)) \cdot sinc(\alpha T(\frac{2R(x)}{c} - \frac{f}{\alpha})) \cdot T \tag{2.26}$$
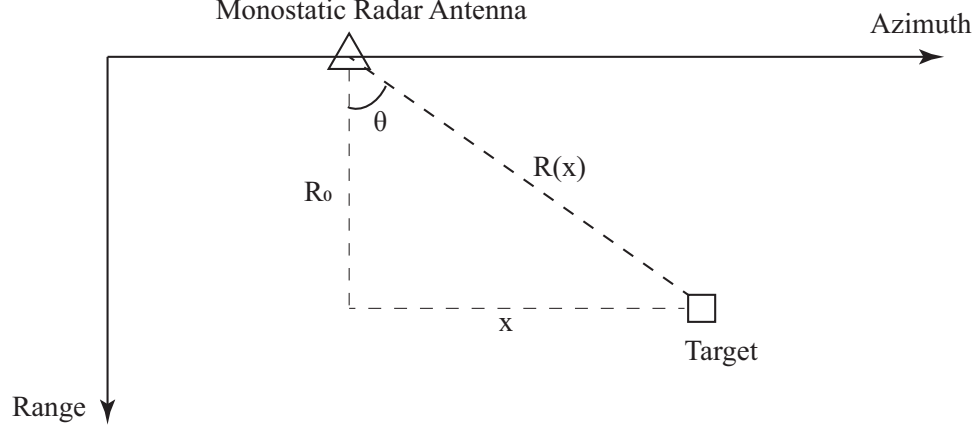
Figure 2.2. Geometry of Radar moving along azimuth

where λ is the center wavelength, c is the speed of light in the medium between Radar and target.

The phase term in (2.26) is wrapped, hence one cannot tell the range $R(x)$ from the phase, however if there are 2 measurements, one can tell the delta range by delta phase. The amplitude envelop in (2.26) is also a function of x, hence one will observe in the range profile, the target draws approximately a hyperbola with opening pointed to the Radar range direction, this is known as Range Migration, or Range Cell Migration (RCM), that has to be corrected before azimuth compression. There are a number of ways to perform Range Cell Migration Correction (RCMC), which will be discussed in the next chapter, simply speaking, those methods perform a mapping between the original range axis to a new range axis.

After RCMC, we consider the phase term in (2.26), and substitute the first 2 terms of the Taylor expansion of $R(x)$:

$$s_{IF}(x) \sim exp(j\frac{4\pi}{\lambda}(R_0 + \frac{x^2}{2R_0})) \tag{2.27}$$

$$= exp(j\frac{4\pi}{\lambda}R_0) \cdot exp(j\frac{2\pi}{\lambda R_0}x^2) \tag{2.28}$$

The first phase term is just a constant, the second phase term has similar form as a baseband chirp signal, where fast time t is substituted by x, chirp rate α is substituted by $\frac{1}{\lambda R_0}$. Hence a matched filtering operation along x will give a sinc function centered at the target azimuth position. Note that according to the above geometry, we were defining $x = 0$ at target azimuth location, so the sinc function will be centered at $x = 0$, which operationally is equivalent to removing the second phase term in (2.28) followed by an azimuth Fourier transform.

It has to be noted that the above calculation is based on one single target, in general the SAR focusing problem is space variant, which means the focusing operation cannot be done by applying a constant kernel over the whole signal space. A number of algorithms are designed to account for this while keeping the efficiency of compression.

2.3.2   Nyquist Sampling

Nyquist sampling theory says when there is a uniformly sampled signal, the maximum frequency that can be reconstructed from the sampled signal is half the sampling frequency.

$$f_{sample} = 2f_{max} \tag{2.29}$$

In the case of azimuth pulse compression, this can be understood as the maximum separation between successive chirps should not exceed a certain amount such that the phase change from the target between the 2 received signal is less than 2π. Obviously it depends on where the target is, more generally the width of the antenna beam pattern in azimuth direction.

2.3.3 Azimuth Resolution

Refer to figure 2.2, and consider the phase of the signal model substituted by $R(x)$:

$$s_{IF}(x) \sim exp(j\frac{4\pi}{\lambda}R(x)) \tag{2.30}$$

$$= exp(j\frac{4\pi}{\lambda}\sqrt{R_0^2 + x^2}) \tag{2.31}$$

Azimuth frequency f_x can be defined by the first derivative of azimuth phase in (2.31) with respect to x:

$$f_x = \frac{\omega_x}{2\pi} \tag{2.32}$$

$$= \frac{1}{2\pi}\frac{d\phi}{dx} \tag{2.33}$$

$$= \frac{1}{2\pi}\frac{d}{dx}(\sqrt{R_0^2 + x^2}) \tag{2.34}$$

$$= \frac{2}{\lambda}\frac{x}{\sqrt{R_0^2 + x^2}} \tag{2.35}$$

$$= \frac{2}{\lambda}sin(\theta) \tag{2.36}$$

where θ is the angle between range axis and the line-of-sight (LOS) between Radar and target.

Azimuth bandwidth is 2 times the maximum azimuth frequency, while the maximum azimuth frequency can be found by substituting θ by half azimuth beamwidth θ_{max}.

$$B_x = 2f_{xmax} \tag{2.37}$$

$$= \frac{4}{\lambda}sin(\theta_{max}) \tag{2.38}$$

The azimuth resolution is simply the reciprocal of bandwidth:

$$\delta Az = \frac{1}{B_x} \tag{2.39}$$

$$= \frac{\lambda}{4sin(\theta_{max})} \tag{2.40}$$

The theoretical maximum azimuth resolution can be found by substituting θ_{max} by 90 degrees, yielding $\lambda/4$. Note that the azimuth sampling frequency has to be denser than azimuth resolution. Therefore, the wider the antenna azimuth beamwidth, the higher the Pulse Repetition Frequency (PRF) required for the same carrier frequency.

2.4 Vector Network Analyzer based SAR systems

There are a number of Vector Network Analyser (VNA) based SAR systems being built by companies around the world, mostly a GBSAR operating on a linear rail of a few meters long [4] [9]. These VNA Radars use similar principles as stretch processing, and operates at a relatively wide band with a lot of flexibility in configuration, like waveform, chirp rate, number of samples, center frequency, etc. Since the core of the Radar transceiver in these systems is just a VNA, these units often operates a much wider bandwidth than other Radars, with the limitation posed by the front-end RF amplifiers and antennas.

Given the flexibility of the VNA based Radar system, it has been very useful in evaluating designs in the research and development stage. Part of the preliminary result of this thesis was generated by a mobile SAR mounted on a truck, where the transceiver was a VNA. One major drawback of the system is the relatively slow PRF, making it non-feasible to put the system into any kind of production on a fast moving platform due to Nyquist sampling requirement along azimuth.

2.5 Software-Defined Radio (SDR) [7] [8]

Software Defined Radio (SDR) is becoming a popular platform for Radio prototyping, in previous generations, due to hardware sampling limits, these devices are

Figure 2.3. A photo showing GBSAR system by LiSALAB

only capable and utilized for the purpose of communication, where the baseband bandwidth requirement is merely a couple to tens of MHz. With the announcement of faster standards including the USB3.0 and PCIe links, together with faster Analog-to-Digital and Digital-to-Analog Converters (ADC and DAC), these Software-Defined platform starts finding its application in the more bandwidth-hungry Radar development.

As an introduction, consider the illustration in figure 3.1, which consist of merely an Antenna, connected to ADC, then to Digital Processor directly, and let alone filters and amplifiers for the moment.

This design is totally nonsense in old days, when the ADC is working in the range of kHz, and at most a few MHz. It is, however, very intuitive to consider this simple model as the basis of today's Software-Defined Radio, where most of the signal processing jobs has been migrated from analog blocks in the RF chain to the Digital Processor (often a general purpose CPU). In fact, every radio system is just a
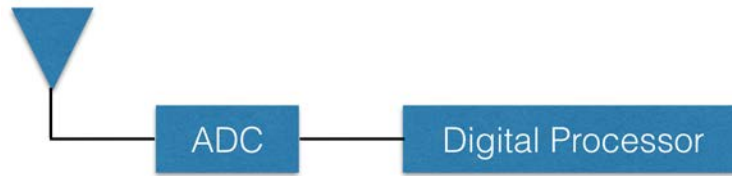
Figure 2.4. Illustration of simplified SDR concept

blending of analog and digital signal processing boundaries. With today's definition, if the whole baseband is being sampled and converted into digital, we call the system Software-Defined.

The second prototype of this research was built based on SDR, details of the design are discussed in chapter 5.

3. SAR FOCUSING ALGORITHMS

3.1 Frequency Domain Methods

SAR focusing methods can be classified into frequency domain based and time domain based. Frequency domain methods are widely used in a lot of production SAR systems as they often make use of the efficient FFT operation in digital signal processing. Here we cover 2 common algorithms: the Range-Doppler Algorithm (RDA), and the Omega-K Algorithm (wKA) [2] [6]. One other algorithm named Chirp-Scaling is also commonly used, for example in the TerraSAR-X, but it requires raw received signal, which is not suitable for the signal model in this research.

In the discussion of algorithms below, we will stay with our signal model described in equation (2.22), and assume the input to the algorithms is the range profiles at each of the azimuth sampling position.

3.1.1 Range-Doppler Algorithm

The Range-Doppler Algorithm is among the first algorithm being used in production SAR systems. The name comes from the axis label during an intermediate step of the algorithm, where the 2D matrix of range profiles are presented in range and doppler (frequency) domain. As we have mentioned earlier, the SAR focusing problem is space variant, meaning the defocus of each of the targets are different, being a function of position and the radar trajectory. This dependence is reduced by presenting the data in the range-doppler domain, hence the image can be focused with a common kernel.

The major steps of Range-Doppler Algorithm is outlined as follow [2] [21]:

- Remove RVP

- Azimuth FFT

- RCMC

- Azimuth Compression

- Azimuth IFFT

Remove RVP

Starting with the signal in (2.22), we first remove the RVP term by point-wise multiplying each of the range profiles with the conjugate of the RVP. Note RVP is a function of range bins.

$$RVP_{correction} = exp(j2\pi\alpha\tau^2) \tag{3.1}$$

Substituting delay time by range, the resultant signal becomes:

$$s_{IF}(f, x) = exp(j2\pi f_0\tau) \cdot sinc(\alpha T(\tau - f/\alpha)) \cdot T \tag{3.2}$$

$$= exp(j\frac{4\pi}{\lambda}R(x)) \cdot sinc(\alpha T(\frac{2R(x)}{c} - f/\alpha)) \cdot T \tag{3.3}$$

Azimuth FFT

Consider the phase term of equation (3.3), take up to second term of Taylor expansion of $R(x)$, and Fourier transform along azimuth from x to f_x:

$$s_{IF}(f, f_x) = \mathcal{F}[s_{IF}(f, x)] \tag{3.4}$$

$$\sim exp(j\frac{4\pi}{\lambda} \cdot R_0(1 + \frac{\lambda^2}{8}f_x^2 - \frac{\lambda^4}{128}f_x^4 + \cdots)) \tag{3.5}$$

where $f_x = 2x/\lambda R_0$ is the azimuth frequency.

From equation (3.5) we can observe the range migration is no longer azimuth position dependent, and the extent of migration is now proportional to the range of nearest approach R_0.

RCMC

RCMC is performed in the range-doppler domain resulted from above step as a mapping along the range axis for each pulse.

$$R_0 \longrightarrow R_0(1 + \frac{\lambda^2}{8}f_x^2) \tag{3.6}$$

After the mapping, the amplitude of the range-doppler signal space should be free of curved lines, but straight lines along azimuth direction.

Azimuth Compression

Azimuth compression can be performed in azimuth slow-time domain as a convolution, or a direct point-wise multiplication to remove the quadratic phase term in the range-doppler domain.

Azimuth IFFT

The last step is to transform the signal from range-doppler domain back to range-slowtime domain. After the operation, the signal has the form:

$$\mathcal{F}^{-1}[r(f_x, t) \cdot exp[j\pi(\frac{\lambda^2}{8}d_x^2 + ...)]] \approx A \cdot exp[j\pi K[t - \frac{2R(x)}{c}]^2]exp[-j\frac{4\pi}{\lambda}R_0] \tag{3.7}$$

Figure 3.1 shows approximately how the amplitude of the signal looks like at each stage of the Range-Doppler process.

It has to be noted that the sketch figure 3.1 assumes the synthetic aperture is long such that the target is being illuminated from one end of the beam to the other end of the beam. Otherwise the azimuth FFT operation will not yield lines along azimuth.

This is because the azimuth signal is proportional to $(x - x_0)^2$, where x is the azimuth position of the Radar and x_0 is the azimuth position of the target. Expanding the square yields x^2, $2xx_0$, and x_0^2. When doing Fourier transform with respect to x, the azimuth frequency is actually proportional to x_0 (or angle of arrival (AOA)) due to the term $2xx_0$. This can be understood like Fourier Optics, where the lens is performing a Fourier transform to convert between the incoming ray intensity at each point on the lens to the AOA of the ray. When the synthetic aperture is long, the

azimuth FFT yields a line because the signal from the same target was recorded by the Radar over a large span of arrival angle. However, when the synthetic aperture is short, over the aperture the target is approximately at the same angular position, hence the azimuth FFT yields an approximately focused target in the range-doppler space, as shown in figure 3.2.
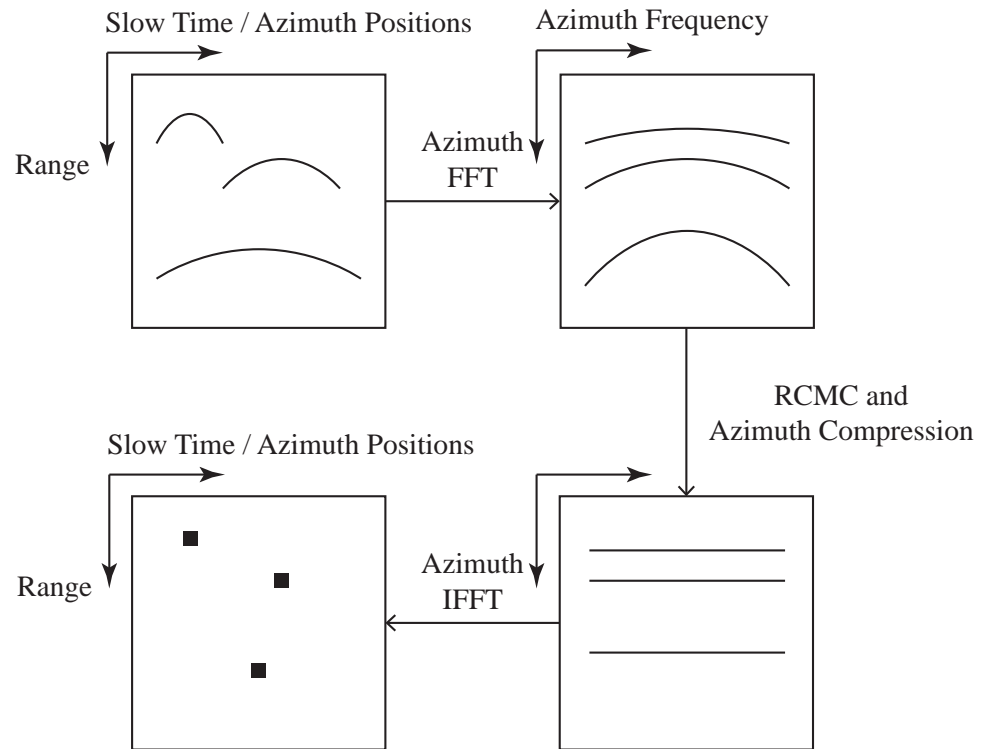
Figure 3.1. The Range-Doppler Algorithm
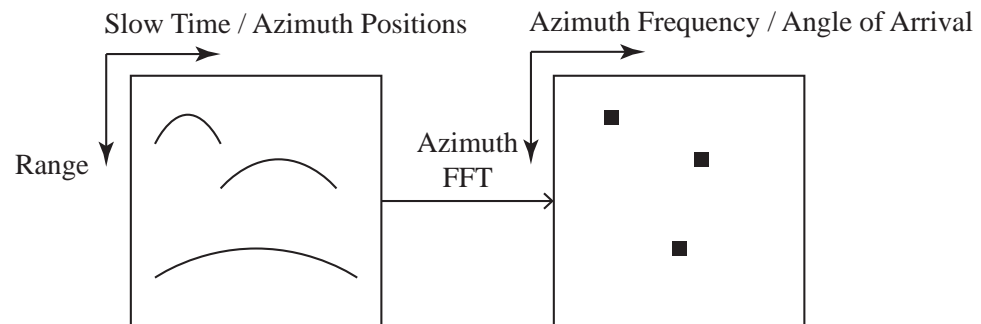
Figure 3.2. The Azimuth FFT of signal from short synthetic aperture

3.1.2 Omega-K Algorithm

The Omega-K algorithm extend the range axis mapping concept in RCMC to 2-dimensional, by converting the signal space and perform the mapping (known as stolt mapping or stolt interpolation) 2D frequency domain, the algorithm can focus a SAR image in less number of steps compared to Range-Doppler method. The name Omega-K comes again from the axis label of the intermediate step where both azimuth and range are transformed into frequency domain, k stands for wavenumber.

The major steps of Omega-K algorithm is outlined as follow [2] [21]:

- 2D FFT

- Multiply with Reference function and Remove RVP

- Stolt Mapping

- 2D IFFT

2D FFT

Consider again the signal model in (2.22), Omega-K algorithm starts by converting the the range profile into 2D frequency domain using a 2D FFT operation. The phase of the signal in 2D frequency space is given by:

$$\phi(f_\tau, f_x) = -\frac{4\pi R_0}{c}\sqrt{(f_0 + f_\tau)^2 - \frac{cf_x}{4}} - \frac{\pi f_\tau^2}{\alpha} \tag{3.8}$$

where f_τ is the range frequency axis; f_x is the azimuth frequency axis; f_0 is the center frequency; R_0 is the range at nearest approach to target.

Reference Function and RVP The next step is to multiply the whole signal phase history with the phase of the reference range, which is also known as the Bulk Compression, or Re-centering. By re-centering, it means taking a certain pixel of the Region-of-Interest (ROI) to be the reference point, and make the phase of the other pixels to be a relative value.

The phase of the signal after bulk compression and removing RVP is:

$$\phi(f_\tau, f_x) = -\frac{4\pi(R_0 - R_{ref})}{c}\sqrt{(f_0 + f_\tau)^2 - \frac{cf_x}{4}} \tag{3.9}$$

Stolt Mapping Stolt mapping is the core of Omega-K algorithm, where a 1D interpolation operation is performed per pulse to map the range frequency axis as follow:

$$\sqrt{(f_0 + f_\tau)^2 - \frac{c^2 f_x^2}{4}} \longrightarrow f_0 + f_\tau' \tag{3.10}$$

where f_τ' is the new range frequency axis.

The phase of the interpolated signal is:

$$\phi(f_\tau', f_x) = -\frac{4\pi(R_0 - R_{ref})}{c}(f_0 + f_\tau') \tag{3.11}$$

Finally a 2D IFFT will bring the signal back to time space in a well focused form. The flow of signal processing is shown in figure 3.3.

3.2 Time Domain Methods

Time domain methods, by its name, performs the focusing in slow time domain and do not perform any Fourier transform along the azimuth direction. These algorithms are known to provide the best focusing quality in terms of the amount of approximation used, for instance the squint angle. The major drawback is the huge computation requirement compared to frequency domain methods, which prevented these algorithms from any practical use until recent advancement in computational power.

Computation requirement aside, time domain method has 2 main advantages over frequency domain methods:

While frequency domain methods are quite reliable in most High-altitude and Space-borne SAR systems, where the platform is stable and trajectory is very linear over the synthetic aperture length, they fails in situation where the trajectory is highly non-linear and when the elevation angle is small, the case when Radar is traveling very close to the ground. Although there were some attempts to perform motion compensation with those images, it is theoretically impossible to fully compensate the error even when the track is exactly know under the frequency domain focusing algorithms. Time domain, on the other hand, handle the signal pulse by pulse, and is able to form the image even when the trajectory is highly non-linear.

The other advantage being no approximation used in squint angles. Frequency domain methods assumes a small squint angle (and small beamwidth), when the squint is large, target far away from the center starts to defocus. There are some modifications being published to account for high squint case, but they are never perfect. Time domain algorithm on the other hand is totally compatible with any squint angle, even when the antenna pointing direction is exactly the forward direction of the platform (forward facing).

For these reasons, the author reckon the importance to use time domain focusing algorithms in ground-based SAR systems with highly non-linear trajectories.
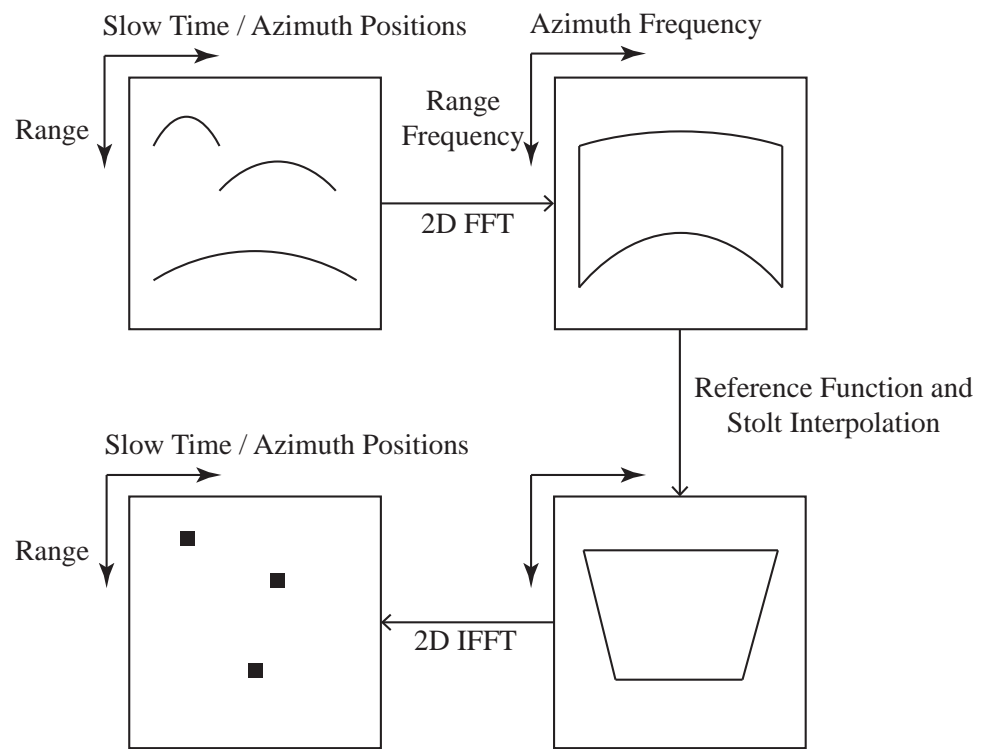
Figure 3.3. The Omega-K Algorithm

3.2.1 Fast Backprojection Algorithm [39]

Fast Backprojection algorithm (FBP) is one of the variant of the Backprojection algorithm. The conventional Backprojection focus the whole image area pixel by pixel. For each pixel, it computes the ranges from each of the antenna pulse location to that pixel, matched-filter each return signal with their corresponding range, and perform a summation over all the pulses, then iterate for the next pixel. This is a tremendous amount of computation, and it is not well-suited for our signal model either, which is pre-compressed in range.

Fast Backprojection takes the range profiles as the layer 1 input, and works very much like range painting shown in figure 3.4. For each of the range profiles, the corresponding antenna position is considered as center of the circle, and the pixels of the image are populated by sweeping the range profile about the center of circle. Repeating this for each pulse yields a constructive interference at pixels where a stable target exists, and destructive interference at pixels where there is nothing in the scene. This is a faster operation over conventional Backprojection by reducing the redundant matched-filtering per pixels [31].
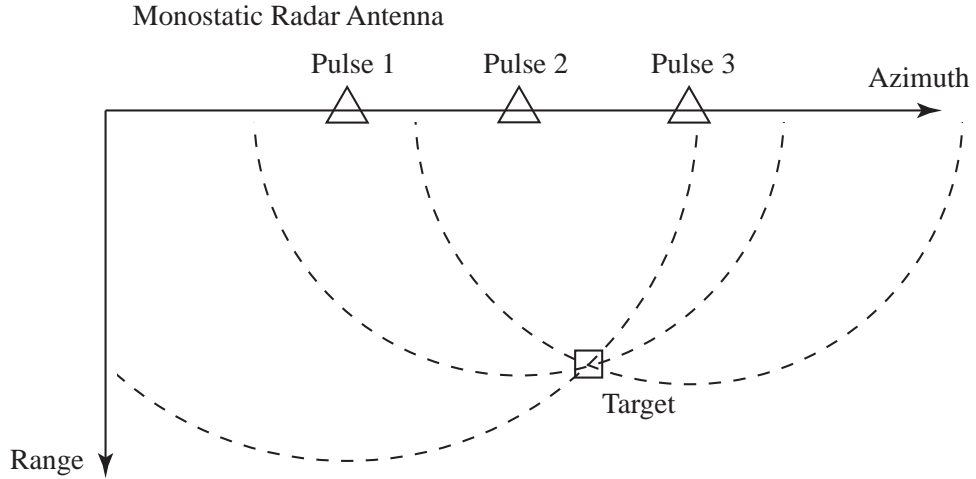
Figure 3.4. Range Painting of Fast Backprojection Algorithm

In practice, the Fast Backprojection do not just paint the image pixel directly, because the range profile grid do not host the signal at exact range to each pixels. An interpolation is used to compute the pixel value contributed by each pulse. Weight is also applied to each pixel as a function of angle of arrivel, this is because the antenna do not really illumulate an isotropic circle around it, but with an amplitude envelop. The steps for Fast Backprojection is outlined as follow:

- Generate image grid with reference to Radar trajectory.

- For each pulse, create an array that store range from antenna location to each pixel.

- Interpolate the range profile to the above array.

- Repeat and sum the image grid for each pulse.

With reference to figure 3.5, when the radar travels along azimuth, the range compressed signal (range profile) can be visualized as a 2D matrix of size (range bins x azimuth pulse). The range from radar antenna position to each pixels is calculated with L2-norm. According to our signal model in (2.22), the signal of each pixel in the focused image can be written as:

$$s_i = \sum_{j=0}^{N} s_j(r = R_{ij}) \cdot exp(-j\frac{4\pi}{\lambda}R_{ij}) \tag{3.12}$$

where i denotes pixel index; j denotes pulse index; R_{ij} is the range from pixel i to pulse j; $s_j(r = R_{ij})$ is the interpolated complex signal of pulse j to range R_{ij}.
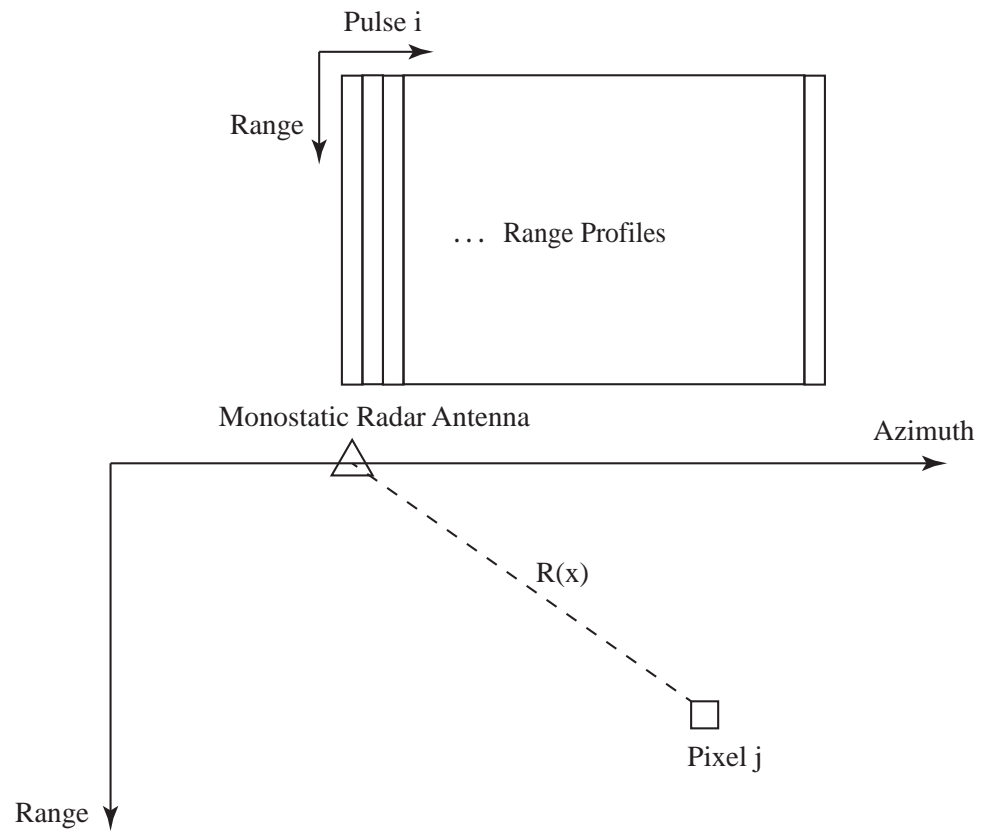
Figure 3.5. Geometry for Fast Backprojection Algorithm

4. VECTOR NETWORK ANALYSER BASED SAR PROTOTYPE [9] [10]

4.1 Background

4.1.1 Problems and Challenges

Existing ground-based SAR (GBSAR) systems are mostly operating at Ku-band or X-band, which has unideal performance when it is used to monitor and detect changes of structures that is partially covered by vegetation due to the poor penetration power of the high carrier freuqnecies [4]. Using a lower carrier frequency allows the target behind vegetation to be illuminated by the Radar beam. Attempts has been made to modify the existing GBSAR systems to operate at L-band, however it requires a longer synthetic aperture which cannot be provided by standard Rail linear positioner.

4.1.2 Solutions

In order to solve the above problem, we have made modification to the GBSAR by replacing the amplifier and antennas that are designed for L-band, we have also removed the Rail positioning solution, and replaced by a GNSS/INS positioning system. The whole system was then mounted at the back of a pick-up truck. SAR dataset was collected and focused successfully.

4.2 The GBSAR system by LiSALAB

Over the past decade ground based synthetic aperture radar (GBSAR) [1] has gain more attention by its ability as a deformation monitoring tool. We evaluated a GBSAR system manufactured by LiSALAB, which utilize a Vector Network Analyzer

as a raddar trasceiver, and bundled with an external modular power amplifier (PA) at the transmit chain, together with a pair of Ku-band horn antenna. Figure 4.1 shows the schematic of the system. The system make use of a stepper motor to position the radar along a 2.7 meters rail, at each position, the radar stops, send the signal and process the echo, then proceed to the next position (stop-and-go approach) [3] [4]. The received signal is de-chirped on receive.
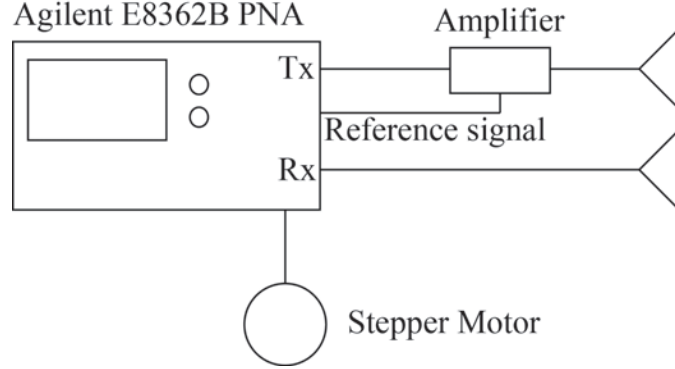
Figure 4.1. Schematic of the LiSALAB Network Analyzer

Consider a 2 port network analyzer where port one is connected to the PA then to the transmit antenna, and port 2 is connected to the receive antenna. The S21 of the analyzer output will be the IF signal, and the range profile can be obtained by doing a FFT operation on the S21 output. The synthetic aperture is formed by knowing the position of the antenna using the stepper motor controls, with the corresponding range profiles at each positions.

4.3 Modifications to the GBSAR system

In the VNA-based prototype, we attempt to take the above mentioned GBSAR system, and apply modifications to get it working on a mobile platform instead of a linear rail. This modification allows flexibility in synthetic aperture length when the system is used with a different antenna configuration and a different carrier frequency.

Consider the expression of azimuth resolution we obtained in (2.40). That azimuth resolution was determined by assuming the synthetic aperture length is not a limiting factor. In the case of GBSAR system operating on a rail of limited length, it is better to express the resolution in terms of angular resolution.

$$\delta Az_{angular} = \frac{1}{r}\frac{\lambda}{4sin(\theta_{max}} \tag{4.1}$$

$$\approx \frac{\lambda}{4r\theta_{max}} \tag{4.2}$$

$$= \frac{\lambda}{2l_{sa}} \tag{4.3}$$

where r is the range; $deltaAz_{angular}$ is the azimuth angular resolution measured in radian; θ_{max} is the half maximum azimuth beamwidth; l_{sa} is the synthetic aperture length limited by length of rail in GBSAR systems.

Assume we have Nyquist sampling requirement fulfilled along the synthetic aperture, which is determined by the carrier frequency and the antenna beamwidth. From the equation, if one would like to keep the azimuth resolution while going from a higher carrier frequency to a lower carrier frequency, a longer synthetic aperture is needed.

In order to improve the vegetation penetration ability of the SAR system, on e has to lower the carrier frequency from Ku-band (the original operating frequency of the LiSALAB GBSAR) to L-band. Lowering the carrier frequency would require a redesign of the SAR geometry including the synthetic aperture. By simple calculation using the above equation, it can be found the rail length required would be too long to manufacture when the system is converted to L-band, hence, it was decided to remove dependence on the rail, and put the system on a mobile platform (i.e. automotive).

4.4 Design of the modified system

The modified SAR system consist of the Vector Network Analyzer (Model: Agilent E8362B PNA) and an Initial Navigation Unit (Novatel Span-CPT). The network analyzer was used as RF signal generator and receiver, which produces a sweep in

frequency, de-modulate and match filter the signal on receive, and give the range-compressed signal in frequency domain at the S21 output. At each pulse, a trigger signal is being sent from the network analyzer to the INS. The INS was set to log the timestamped position XYZ at 20Hz, as well as time-stamp whenever a trigger is received. Schematic of the system is shown in figure 4.2.

It should be noted that a major limitation of this system is the data read out rate of the Network Analyzer, which limits the pulse repetition interval (PRI) to the range of 0.1 - 0.5 seconds. As a result, the system can only be used as an evaluation while not being able to operate on a fast moving platform. The setup was installed on a pick-up truck during experiment, shown in figure 4.3.
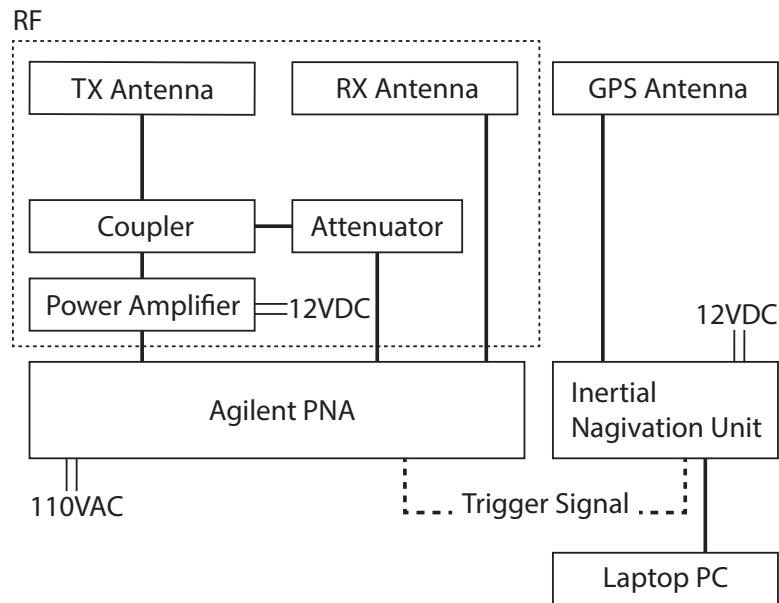
Figure 4.2. Schematic of the modified VNA-based SAR system

4.5   Example Imagery

We present 2 set of SAR image collected using the modified mobile SAR system.

Dataset 1 For the first example, data was acquired in a parking lot of Purdue University, West Lafayette. The frequency output was set to be 1.7GHz to 2.0GHz with a bandwidth of 300MHz, equivalent to a range resolution of 0.5 meters. The -3dB beamwidth of antenna is 13.3 degree, thus equivalent azimuth resolution is about 0.13 meters.

The range profiles was collected on an approximately linear track. The pulse timing was determined by the PNA unit, which is uniform. The global timing and positioning solution was provided by the attached GNSS/INS system, which create a record whenever a trigger signal is received. The recorded timing and position is the interpolated value from the sensor measurement. Since the track was not perfectly uniform, motion compensation was performed in the azimuth direction to interpolate the range profiles along a uniform azimuth space using the positioning data. Range Doppler algorithm was used to focus the dataset in azimuth, and the steps are as outlined in section 3.1.1. Figure 4.4 shows the image (not-to-scale) compressed by RDA, and figure 4.5 shows the image (to-scale) overlay on google earth imagery.

Figure 4.3. Modified VNA-based SAR system installed on truck
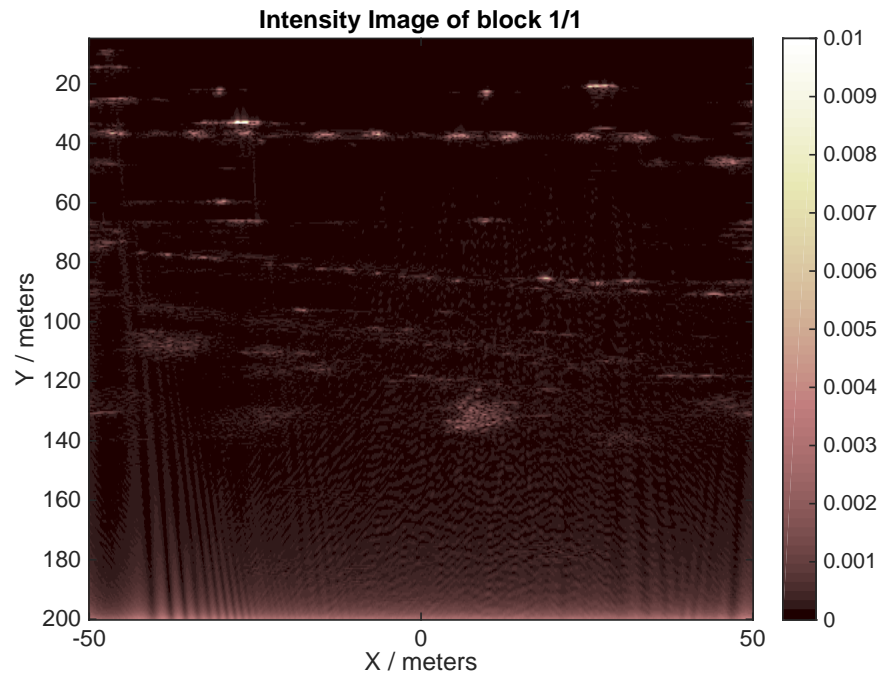
Figure 4.4. Focused SAR image

Dataset 2 The second dataset was acquired in an open area at south part of Purdue University, West Lafayette. The radar parameters are the same as dataset 1. The resultant image is shown in figure 4.6
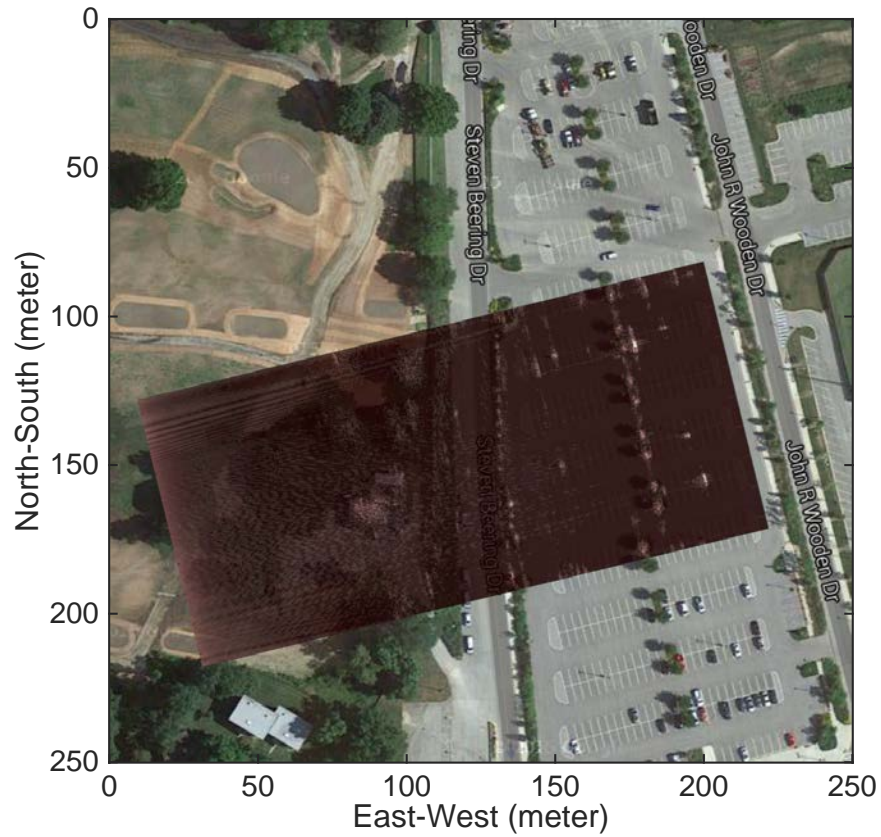
Figure 4.5. Focused SAR image (dataset 1) overlay on Google Earth

4.6   Discussion

As shown in the example imagery, the modified SAR system operating in L-band on a mobile platform works as expected. However there are some limitations that we want to overcome:

Cost

The cost of using a PNA in SAR system is expensive. PNA is designed for laboratory measurement, with a lot of flexibility in tuning the waveform, and a high precision in measurement. While these characteristics are nice in the prototype stage for debugging and research purpose, it is hard to be put into practical use.

Pulse Rate
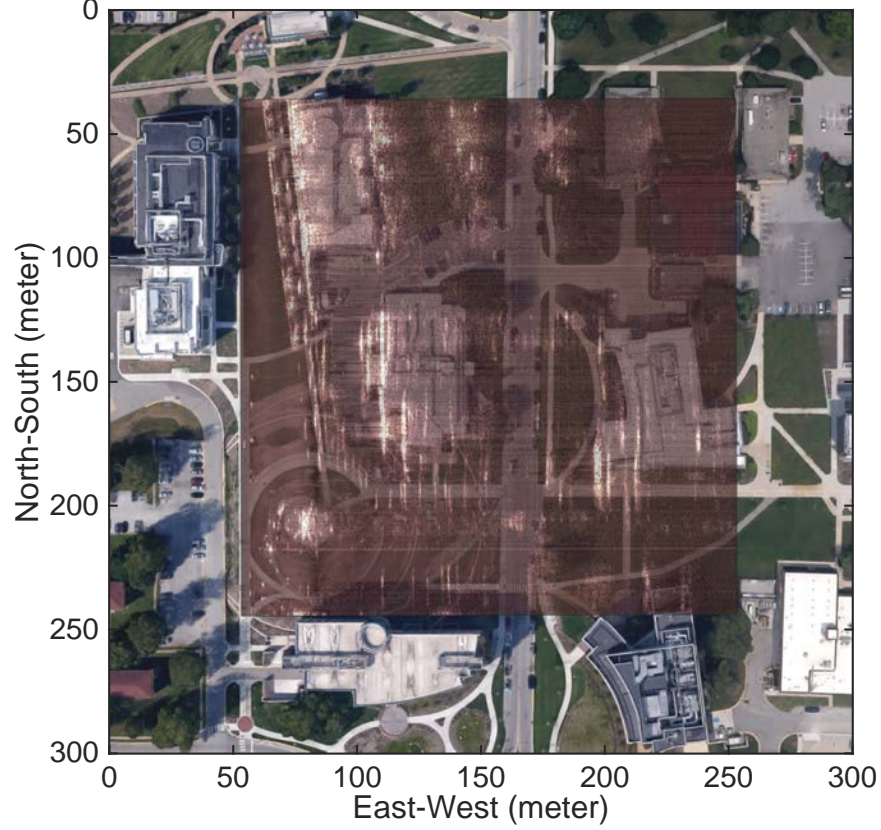
Figure 4.6. Focused SAR image (dataset 2) overlay on Google Earth

The use of PNA in SAR pose a limitation in the pulse repetition frequency. This was because PNA was not designed for very fast measurements. As a result, the maximum traveling speed of the radar platform is limited due to the Nyquist sampling requirement along azimuth.

Non-linear Track

In the above example datasets, we attempted to keep the track as linear as possible while driving, and any variation in speed was compensated by in interpolation along azimuth pulses using the position information obtained from the GNSS/INS system. Although there exist some methods to compensate for range motion, those methods are only applicable to far-range ROI, and does not work for the ground-based system which ROI starts at range zero. In order to correct for this, one should consider the

use of time-domain algorithm like the Backprojection algorithm instead of the Range Doppler algorithm.

Given the limitation in cost and pulse rate, the author propose the use of software-defined radio (SDR) systems to replace the PNA. The SDR-based system was assembled and its basic Radar functionality has been demonstrated and is discussed in the next chapter.

5. SOFTWARE DEFINED RADIO BASED RADAR PROTOTYPE

5.1 Background

5.1.1 Problems and Challenges

Following the implementation of the first SAR prototype, there were 2 problems, firstly, the Network Analyzer based transceiver was very slow, which limited the PRF and hence the maximum speed of the radar platform. Second, the lack of MIMO capability has limited the implementation of advanced autofocusing techniques that are discussed in chapter 6-7.

5.1.2 Solutions

With the above considerations, we have decided to replace the transceiver in the first prototype by the Software Defined Radio (SDR) transceiver, which should be able to provide a higher data rate, as well as MIMO capability. We have also redesigned the signal processing chain to allow the carrier frequency of the SDR transceiver to be tuned while keeping phase coherence, such that the bandwidth of the system can be increased for a better range resolution.

5.2 System Overview

5.2.1 The B210 by Ettus Research [7] [8]

The USRP (Universal Software Radio Peripheral) B210 by Ettus Research, shown in figure 5.1, was chosen for use in the prototype, mainly based on the following reasons:

- Coverage in the L-band

- 2TX and 2RX MIMO configuration

- USB3.0 Link

- Small form factor

- Small power consumption

Figure 5.1. A photo of B210

Some of the key specifications of the B210 is tabulated as follow:

Detail specification of USRP B210 can be found on

`https://www.ettus.com/content/files/b200-b210_spec_sheet.pdf`

The hardware blocks inside the USRP B210 is shown in figure 5.2. The USB3.0 is to be connected to a general purpose PC where a software has to be run in real time for generating and pre-processing the baseband signal (more discussion on this will be given in next section). The baseband signal goes through a pre-programmed FPGA chip which act as DUC (Digital Up Converter) and DDC (Digital Down Converter)

Specifications	Typ.
RF coverage	70MHz - 6GHz
Interface	USB3.0
FPGA	Xilinx Spartan 6 XC6SLX150
Instantaneous bandwidth	Up to 56MHz in 1x1, 30.72 in 2x2
ADC and DAC Sample Rate	61.44MS/s
ADC and DAC Resolution	12 bits
Frequency Accuracy	$\pm$ 2.0ppm
Phase noise @ 3.5GHz	1 deg RMS
Power Output	>10 dBm
DC Input	6V
Weight	350g

for sampling rate conversion, then pass into the RFIC and front-end RF network. The DAC/ADC is performed by AD9361 chip supplied by Analog Device, the schematic is shown in figure 5.3.
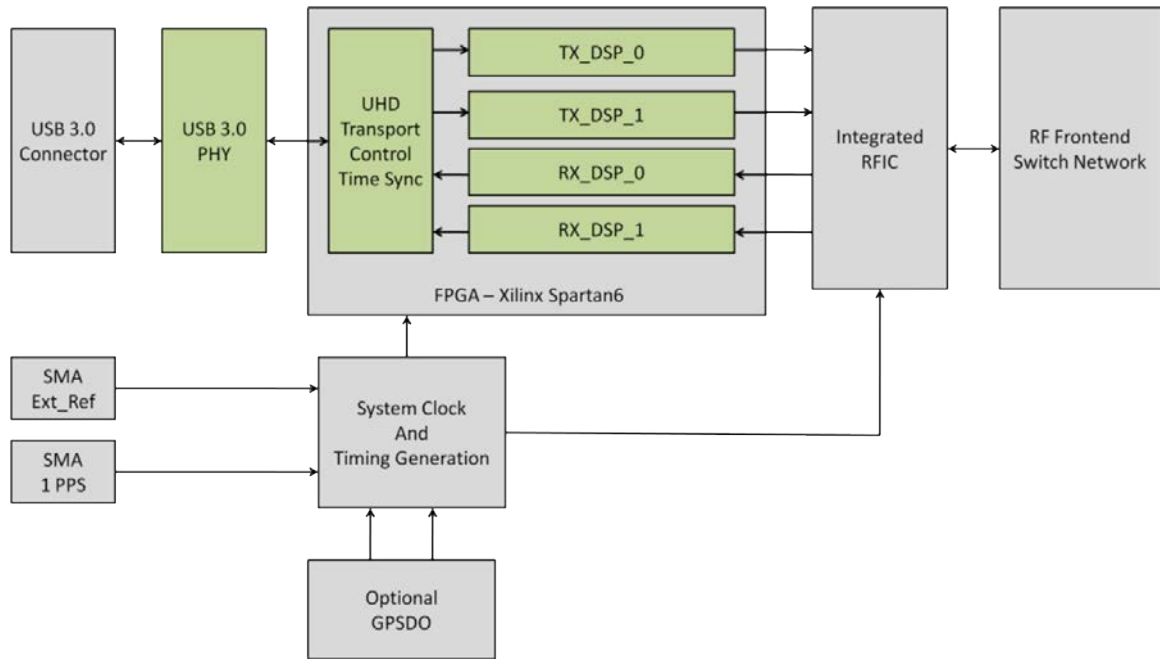
Figure 5.2. Inside the USRP B210

5.3 The RF Frontend

The implementation of amplifier circuit on an USRP is relatively simple. In the design, an unconditionally stable broadband power amplifier (PA) (Model: ABP0600-07-3629) and unconditionally stable boardband low noise amplifier (LNA) (Model: ABL0200-50-3516) supplied by Wenteq was chosen. The transmit port (labelled as TX1) is connected to the input of PA, then to a Directional Coupler with a -30dB coupling port feeding back to a receive port (RX1), and port 2 of the directional coupler connected to the TX antenna. The signal from RX antenna goes through the LNA to another receive port on the USRP (RX2). A simplified sketch is shown in figure 5.4, note the voltage bias and attenuators are not shown.

Assuming typical values, the output at USRP TX1 is 10dBm, the PA has 36dB gain at room condition, with -10dB attenuators, the transmitted power is approximately 36dBm = 4 Watts.

RX1B_P, RX1B_N
RX1A_P, RX1A_N
RX1C_P, RX1C_N
RX2B_P, RX2B_N
RX2A_P, RX2A_N
RX2C_P, RX2C_N
TX_MON1
TX1A_P, TX1A_N
TX1B_P, TX1B_N
TX_MON2
TX2A_P, TX2A_N
TX2B_P, TX2B_N
SPI
CTRL

AD9361

RX LO
TX LO

DATA INTERFACE

ADC
ADC
DAC
DAC

P0_[D11:D0]/ TX_[D5:D0]
P1_[D11:D0]/ RX_[D5:D0]

CTRL
ADC   DAC   DAC
GPO   RADIO SWITCHING
PLLs   CLK_OUT

AUXADC   AUXDACx   XTALP XTALN

NOTES
1. SPI, CTRL, P0_[D11:D0]/TX_[D5:D0], P1_[D11:D0]/RX_[D5:D0],
AND RADIO SWITCHING CONTAIN MULTIPLE PINS.

10453-001

Figure 5.3. Schematic of AD9361

The receiver noise figure of USRP B210 is less than or equal to 8dB, while the LNA has typ. noise figure of 1.6dB and gain of 35.5dB, the equivalent noise figure of the receiver chain is 1.604dB.

Detail specifications of amplifiers and antennas can be found in the appendix.

5.3.1   Mountings

Based on the development and calculation in previous chapters, the hardware part of the prototype was implemented and assembled. The hardware was designed with multiple DC voltage up/down converters and regulators such that it can be operated on a laptop with USB link and a single 12V lead-acid battery, without the need of other external power supply. A photo of the prototype is shown in figure 5.5 and 5.6.
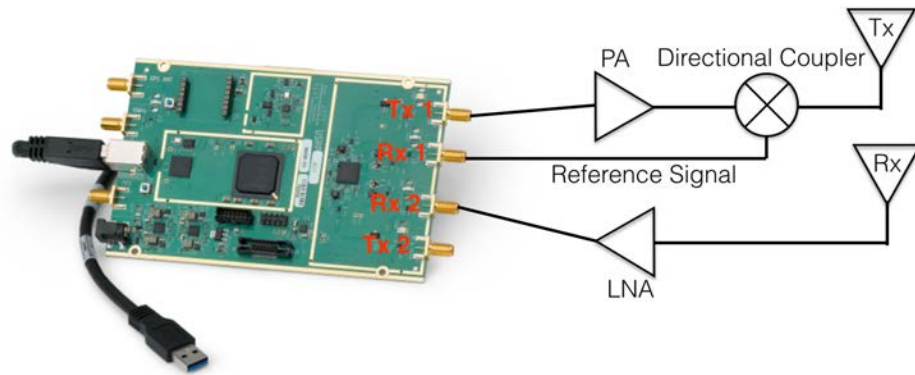
Figure 5.4. Illustration of Amplifier and Antenna connections on the USRP B210

5.4 A Simple Radar under the GNU Radio Framework [7]

Under SDR framework, the host PC is responsible for generating and receiving the whole baseband signal. These signals are generated in complex float (complex64), and transformed into OTW format (Over-The-Wire) in sc16 or sc12 before sending to the USRP.

This signal processing software can be implemented using the GNU Radio framework, or using the C++ API of the UHD (USRP Hardware Driver). Some of the comparison and functionalities are given as a brief preview, and an example of simple Radar implementation using the GRC (GNU Radio Companion) is also given for illustrating the basic steps of realizing a Radar from signal generation to range compression.

GNU Radio is a software specifically developed for signal processing, which works not only on RF, but also acoustics, allowing developers and educators to implement designs on various hardware like USRPs or even Laptop microphones and speakers. Behind the software is a library of signal processing blocks written in C and Python, including the common FFT, Hilbert Transform, AM/FM Modulation etc. While the

Figure 5.5. SAR Proto-
type (back)

Figure 5.6. SAR Proto-
type (front)

library is large, some functions that is not available in the library can be written by users using C or Python and added to the software with a tool in terminal, which are called Out-Of-Tree (OOT) blocks. GNU Radio controls the USRP via the USRP Hardware Driver.

An simple Radar is implemented as example using the GNU Radio, and the block diagram is given in figure 5.7. In the implementation, a vector source is used to generate the baseband up chirp, the signal is Hilbert transformed to complex signal, and transmitted using a USRP sink at carrier frequency of 1.2GHz and sampling rate of 20.48MS/s. The received signal is Fourier transformed and multiplied with the complex conjugate of a copy of the transmitted signal, which is the stretch processing outlined in section 2.2.1. The resultant waveform is transformed back into time domain for visualizing a peak in the received signal, which position correspond to the delay of echo after hitting the target.
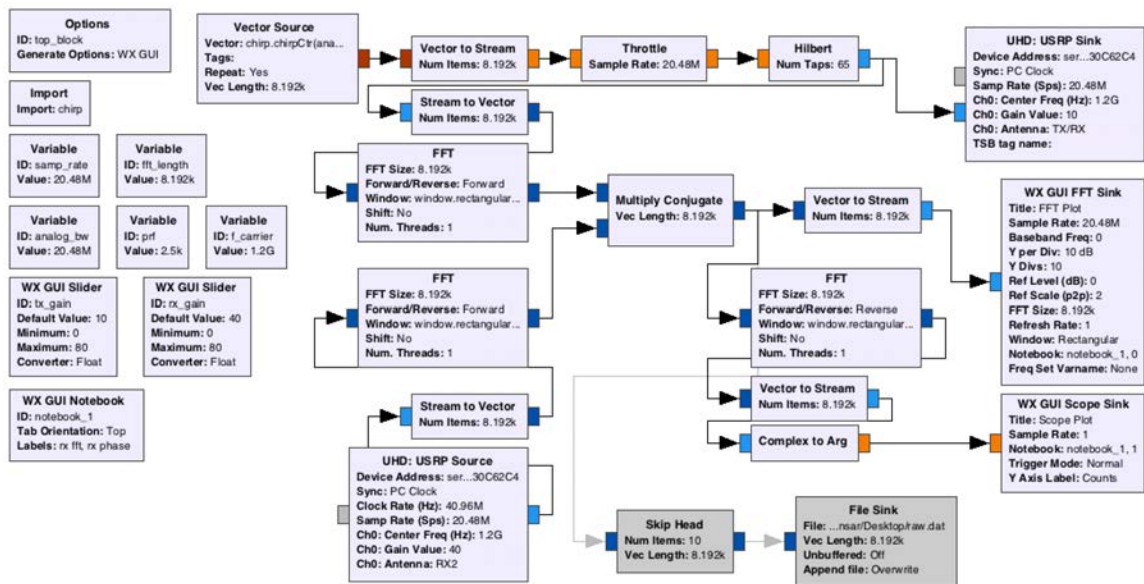
Figure 5.7. Block diagram of a simple Radar implemented on GNU Radio Companion

The result shown in figure 5.8 is the amplitude response in time domain, and the result shown in figure 5.9 is the phase response in frequency domain.
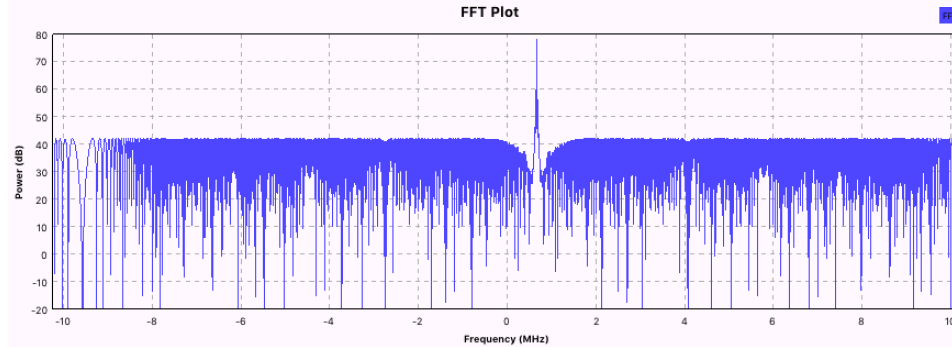
Figure 5.8. Amplitude Response in Time Domain
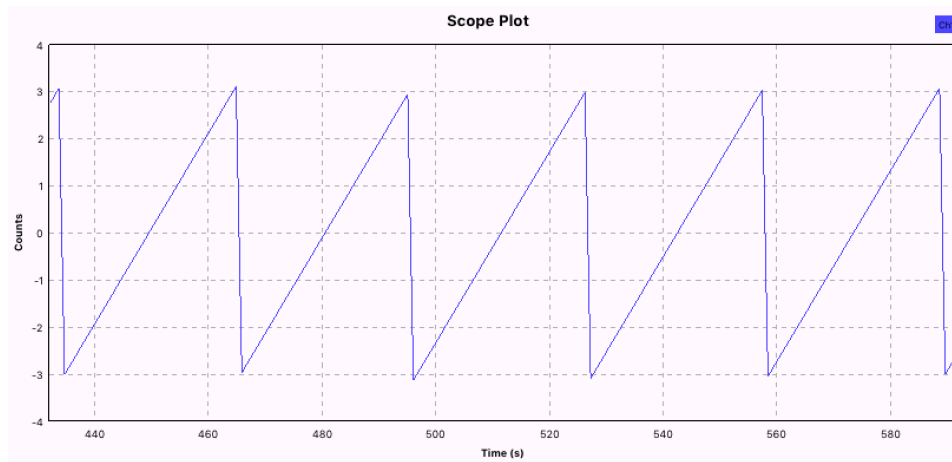
Figure 5.9. Phase response in Frequency Domain

It has to be noted that the final implementation of the Radar prototype is not be based on the GNU Radio framework, instead using the C++ API of UHD, mainly due to the following reasons:

1. The GNU Radio framework limits the capabilities of USRP as it runs in a flow graph and parameters cannot be dynamically tuned, this impact is especially important because carrier tuning is to be implemented in the design of this prototype.

2. The signal processing under GNU Radio might not be as fast as that implemented directly on the C API of UHD.

5.5   Carrier Frequency tuning in USRP

The current USRP specifications is still not ideal for a Radar application, especially with the limited sampling rate (30.72 in 2x2 MIMO), hence limited baseband bandwidth and range resolution. Stretch processing [15] [37] [38] is one way to work around with limited baseband bandwidth, here another method is proposed, based on tuning the carrier frequency on the fly.

There are 2 non trivial problems to be solved for tuning the carrier, firstly the tuning time. According to Ettus Research, the tuning time is less than 1ms and depends on how far the new frequency is from the original frequency. The second problem is the Radar requires signal to be coherent, while tuning often change the phase and frequency with some uncertainties. To explain the second problem, we need to take a deeper look into AD9361.

With reference to the schematics of AD9361, both receiver chain shares the same RX LO, and both transmitter chain shares the same TX LO. Given that there will be some uncertainty in the phase of each LO after a tuning, $\Delta\phi_1$ and $\Delta\phi_2$, and a unknown frequency difference between the TX LO and RX LO, $\Delta\omega_n$, consider a simple case where a single tone baseband signal is being transmitted:

$$s(t) = exp(i2\pi f_0 t) \tag{5.1}$$

The result of modulated and received signal can by found by simplifying the schematics of AD9361 to outline the IQ modulation part, shown in figure 8.10, where

$\Delta\omega_n = \Delta\omega_1 - \Delta\omega_2$, and double arrow indicates complex IQ signal, single arrow indicates real physical signal.

The transmitted RF signal after passing the TX LO (after filtering) is

$$Tx(t) = Re[s(t)]cos(2\pi f_n t + \phi_1) + Im[s(t)]cos(2\pi f_n t + \phi_1) \tag{5.2}$$

$$= cos(2\pi(f_n - f_0)t + \phi_1) \tag{5.3}$$

Hence the corresponding reference and received signal after passing the RX LO is

$$ref(t) = cos(2\pi(f_n - f_0)t + \phi_1)cos(2\pi(f_n + \Delta f_n)t + \phi_2) \tag{5.4}$$

$$+ icos(2\pi(f_n - f_0)t + \phi_1)sin(2\pi(f_n + \Delta f_n)t + \phi_2 \tag{5.5}$$

$$= \frac{1}{2}exp[i(2\pi(f_0 + \Delta f_n)t + \Delta\phi)] \tag{5.6}$$

$$rx(t) = cos(2\pi(f_n - f_0)(t - t_0) + \phi_1)cos(2\pi(f_n + \Delta f_n)t + \phi_2) \tag{5.7}$$

$$+ icos(2\pi(f_n - f_0)(t - t_0) + \phi_1)sin(2\pi(f_n + \Delta f_n)t + \phi_2 \tag{5.8}$$

$$= \frac{1}{2}exp[i2\pi(f_0 t + (f_n - f_0)t_0 + \Delta f_n t + \Delta\phi)] \tag{5.9}$$

where $\Delta\phi = \phi_1 - \phi_2$.

Mixing $rx(t)$ with $ref(t)$, the uncertainty Δf and $\Delta\phi$ are canceled out and the output signal $s_{out}(t)$ is given as:

$$s_{IF}(t) = rx^*(t)ref(t) \tag{5.10}$$

$$= const \cdot exp[i2\pi(f_n - f_0)t_0] \tag{5.11}$$

Equation (5.11) describe the signal in every LO frequency f_n, which should be of length equal to that of the transmitted baseband waveform, and the phase for each sample being constant over the length of signal if the baseband is a Sine waveform.

Performing Fourier transform to a the signal described by equation (5.11) across different LO frequencies f_n yields the range compressed signal:

$$S_{out}(t') = \sum_m const \cdot exp[-i2\pi(f_c)t_0]sinc(T(t' - \tau_m)) \qquad (5.12)$$

where t' is the delay-time axis; f_c is the center of the carrier frequency tuning; τ_m is the delay to the target m.

Consider the above measurement is repeated with different carrier frequency ω_n for n = 1...m, and each outputs a function denoted in equation (5.12), the resultant signal can be added together in the frequency domain base on the fact that each signal is located at unique frequencies, and the result is illustrated in figure 5.11.

An inverse Fourier transform operation of the signal in figure 5.11 should bring back to the time domain signal with an effective bandwidth from f_1 to f_m.
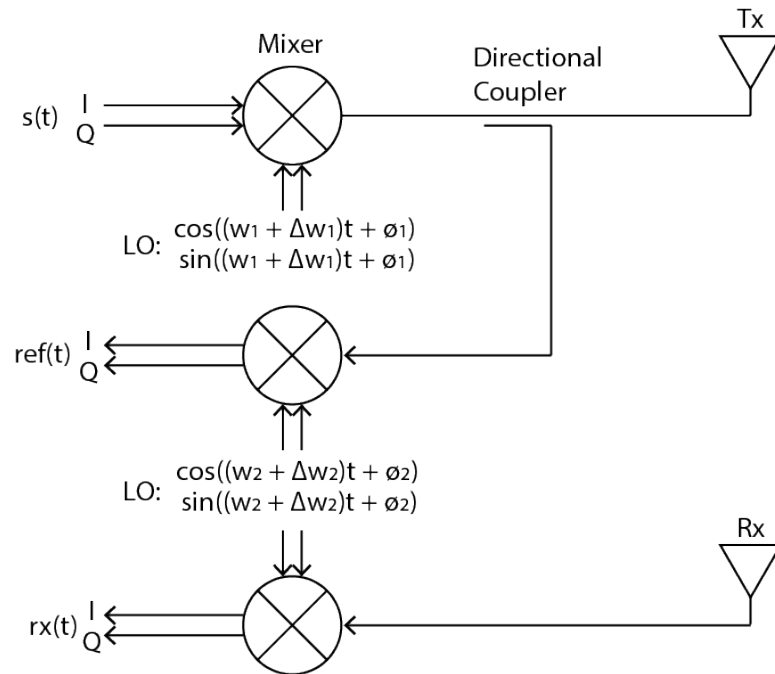
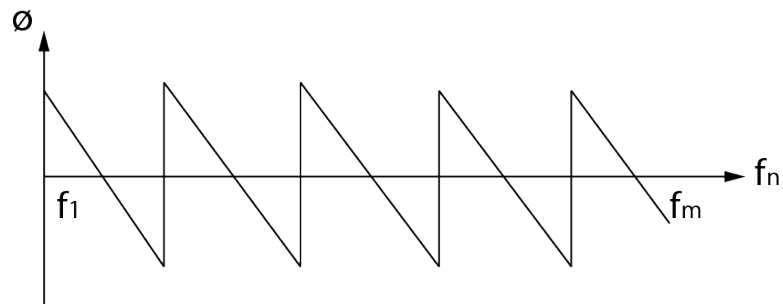Figure 5.10. Illustration showing the IQ modulation part of AD9361

Figure 5.11. Illustration showing the combined signal in frequency domain

5.6 Results

The carrier frequency tuning was implemented under the C++ API provided along with the UHD driver by Ettus Research. The B210 Radar was programmed to operate in 1TX and 2RX configuration, and transmit a fixed baseband frequency in form of a sinc wave, modulated with a carrier frequency which step up from 1.1GHz to 1.3GHz. The transmitted signal was split into 2 stream, one being sent to the TX antenna, another one loopback to RX0. The RX antenna is connected to RX1.

The transmit and receive stream of signal is modulated by specified start and end carrier frequency in linear steps. The 2 received stream are saved locally on the host computer, and mixed to remove the frequency and phase deltas as discussed in equation (5.9). The resultant signal would be of length (N x M) where N is the sample length of the baseband signal per frequency step, and M is the number of frequency step. Ideally the phase of the signal within the same baseband should be constant if the baseband waveform is a sine function. Therefore, the range profile is obtained by an FFT operation along the M dimension, i.e. across the carrier frequencies.

A dataset was collected at a test scene shown in figure 5.12, and the resultant range profile is shown in figure 5.13. The Radar parameters are as follow:

- Start Frequency: 1.1GHz

- Stop Frequency: 1.3GHz

- Bandwidth: 200MHz

- Range Resolution: 0.75 meter

- Frequency Steps: 50

- Max Range: 37.47 meters

There are 3 major objects that can be identified from the range profile: A small part of the wall at range 1 meter, a corner reflector at range 6.3 meter, and another

wall at range 16 meters. The range of the object is verified by a laser range finder with 0.01 meter precision.

Since the signal from the antenna is spreading quite wide given the low carrier frequency, a lot of other objects were being caught into the range profile, never the less, we can identify a significant peak located at the position of the 3 features above. Moreover, it should be noted that theoretically there is no signal returning from behind the wall at range 16 meters, hence after the 16 meters peak, the signal showed a sinc-like feature.
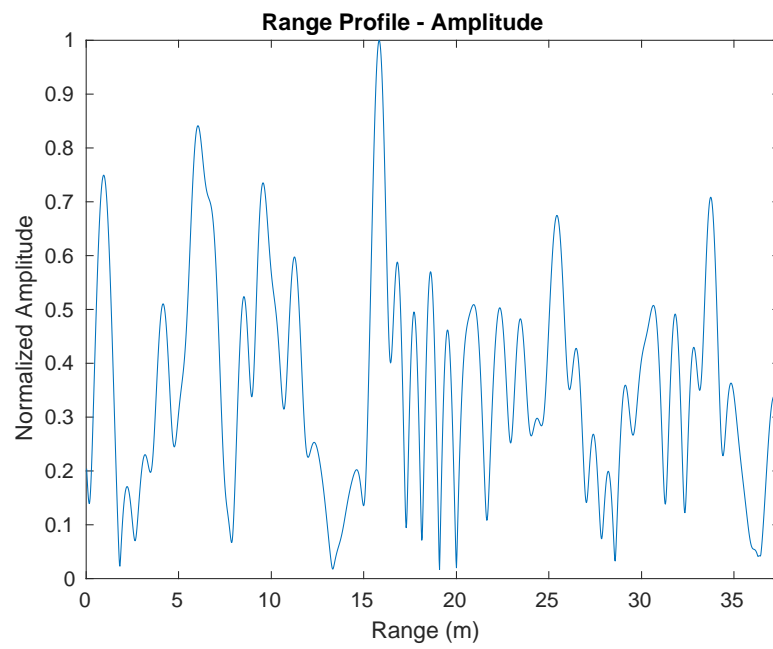

Figure 5.12. Photo showing the test scene

Figure 5.13. Amplitude of the Range Profile

6. MODIFIED PHASE GRADIENT ALGORITHM (PGA)

6.1 Background

6.1.1 Problems and Challenges

As we have mentioned in previous chapters, implementing a SAR systems on an unstable platform poses a lot of challenges in timing and positioning, which was the key to define the signal compression kernel in the focusing algorithm. Very often we do not have accurate knowledge of the position information, which manifest to a blurry SAR image. There are existing autofocusing algorithms [28] [29] [30] designed to correct for these type of blurring in SAR image by analyzing the phase history of the image, identifying the component in the phase which is from the actual target signal, and separate it from the noise component. For instance, we consider the Phase Gradient Algorithm (PGA) [32]. Despite its robustness, the stock PGA cannot be applied directly to our system. Potential problems include the SAR geometry, time or frequency domain algorithm being used, and whether spotlight or stripmap configuration is being used.

6.1.2 Solution

To correct for the 3 problems listed above, we have redesigned the Phase Gradient Algorithm. Additional processing steps are added to convert dataset between stripmap and spotlight, as well as correcting for the phase of image focused with time-domain algorithm. A motion model has been added to account for the near-range geometry, such that a differential phase correction is applied to each range bins depending on where the target is located, compared to the single averaged phase correction in the original PGA. The result has shown great improvement in sharpening

the SAR image when using the Modified PGA compared to the stock PGA in our specific SAR configuration.

6.2 The Conventional PGA

The Phase Gradient Algorithm (PGA) is shown to be a robust autofocusing algorithm used in many SAR signal processing systems [22]. It does not assume any error model for the phase compared to algorithms like map-drift [24], and performs well in low contrast scenario. PGA works by analyzing the phase history (along azimuth) for each of the dominant target, the common variation in phase history is said to be the phase error to be removed. In the following discussion, we assume the input to PGA is a pre-focused image with a little blur along azimuth.

6.2.1 Processing Steps

There are 4 major steps in Phase Gradient Algorithm:

- Circular shift

- Windowing the dominant target

- Estimate the phase error using phase gradient

- Remove the phase error and iterate

Circular shift

We consider the azimuth signal model from a spotlight SAR configuration to be:

$$g_n(t) = A_n \cdot exp(-j(\omega_0 t + \phi_e(t) + \phi_0)) + \eta(t) \tag{6.1}$$

where n is range bin index; A_n is the amplitude; ω_0 is the frequency of the signal; $\phi_e(t)$ is the slow-time dependent phase error to be estimated; ϕ_0 is the remaining constant phase.

The azimuth Fourier transform of equation (6.1) yields:

$$G_n(\omega) = A_n \delta(\omega - \omega_0) \cdot exp(j(\phi_0) * E(\omega) * \Gamma(\omega)$$ (6.2)

where $E(\omega)$ and $\Gamma(\omega)$ area the Fourier transform of the phase error and noise term respectively.

Note that from equation (6.2) the constant frequency term ω_0 is actually the position of the target in the frequency domain. Hence, by circular shifting the image along azimuth in the frequency domain such that the dominant target is at the center of the image, we are removing the constant frequency term.

The azimuth signal in slow time domain after circular shifting is:

$$g_n(t) = A_n \cdot exp(-j(\phi_e(t) + \phi_0)) + \eta(t)$$ (6.3)

Windowing

Next, we apply windowing about the center of the image in the frequency domain. The windowing operation removes any phase contributed by other targets in the same range, which is denoted as noise in the single target azimuth signal model in (6.1).

The window size has to be carefully designed such that it includes any phase information of the blurred dominant target but not that of other minor targets.

The signal in slow time domain after windowing has the form:

$$g_n(t) = A_n \cdot exp(-j(\phi_e(t) + \phi_0))$$ (6.4)

Estimate phase error At this point, the only slow time dependent term in the signal model is $\phi_e(t)$. To estimate the phase error, we differentiate (6.4) with respect to t:

$$\dot{g}_n(t) = A_n \cdot -j\dot{\phi}_e(t) exp(-j(\phi_e(t) + \phi_0))$$ (6.5)

$$= -j\dot{\phi}_e(t) g_n(t)$$ (6.6)

Hence we can estimate $\dot{\phi}_e(t)$ by:

$$\dot{\phi}_e(t) = -j\frac{g_n(t)^H \dot{g}_n(t)}{g_n(t)^H g_n(t)} \tag{6.7}$$

The final estimate is computed by taking all range bins n into account:

$$\dot{\phi}_e(t) = \frac{\sum_n Im[g_n(t)^H \dot{g}_n(t)]}{\sum_n |g_n(t)|^2} \tag{6.8}$$

The phase gradient $\dot{g}_n(t)$ can be computed using the Fourier transform relation:

$$\mathcal{F}^{-1}[j\omega G(\omega)] = \dot{g}(t) \tag{6.9}$$

Remove phase error and iterate

The phase error computed in previous step is a function of slow time (t), therefore an azimuth Inverse Fourier transform is applied to the input image before multiplying with the phase error correction term, and a Fourier transform afterward to bring signal back to image domain. Note that the same phase error correction is applied to each range bins. A flow chat is shown in figure 6.1 outlining the PGA steps.

6.2.2   Limitations

Works on Spotlight SAR [23] [34]

The original PGA assumes input data is collected in spotlight configuration, where the range profiles is obtained by match filtering to the same scene center. That means the data has minimal or no RCM, and the target is illuminated and observable over the whole aperture.

This is not true for data collected in stripmap configuration, which is the operation mode of the prototype in this research. In stripmap mode, RCM is observable in range profiles, and some target disappears mid way due to illumination pattern.

Works on frequency domain focused images [31]

PGA assumes the image is focused using frequency domain algorithms like RDA or wKA. These algorithms has a uniform support/kernel of focusing for each of the pixels, hence each pixels has the same image spectrum.

However, in time domain algorithms like the Backprojection, the support of each pixel are different, causing the spectrum to be misaligned. The idea is visualized in the sketch in figure 6.2, where a 2D FFT of different sub-region 1-3 do not yield perfectly overlapping spectrum support in the frequency domain. The spectrum misalignment simply means the azimuth signal model in equation (6.1) no longer holds, hence PGA cannot be applied.

Geometry only designed for high-altitude SAR

The third limitation, also the most significant one, is about the geometry of the SAR acquisition system. PGA was designed for high-altitude SAR system, which has a very long range between radar antenna to scene center (R_0), and a relatively small ROI. As a result, any phase error caused by irregular motion of the radar platform has approximately the same effect on the phase of all the range bins. This is also the theoretical basis of the summation operation in equation (6.8).

Obviously, this is not true for most ground-based system where the starting range is often zero (i.e. R_0 ROI). For instance, consider a sudden shift in position in range,
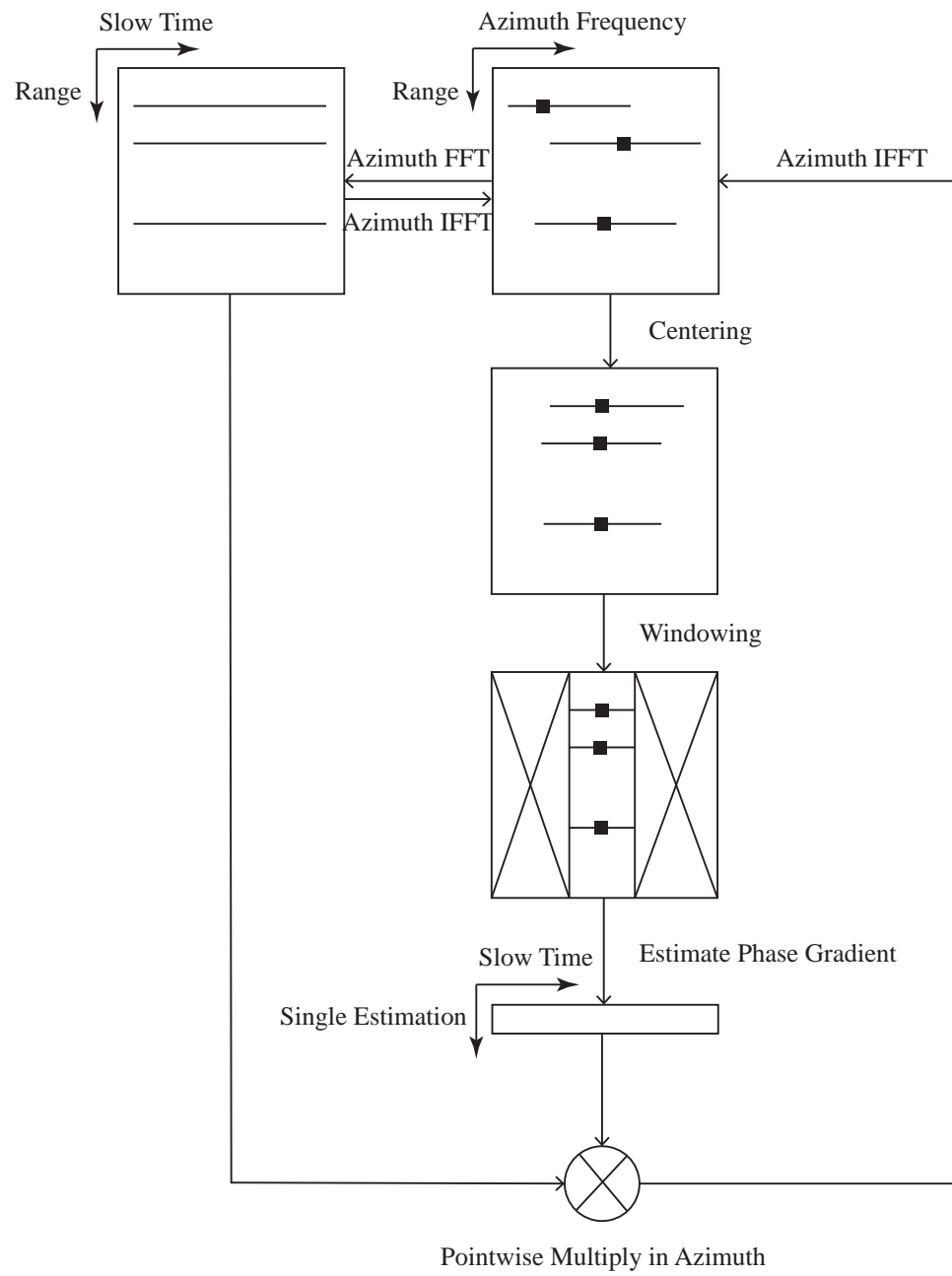
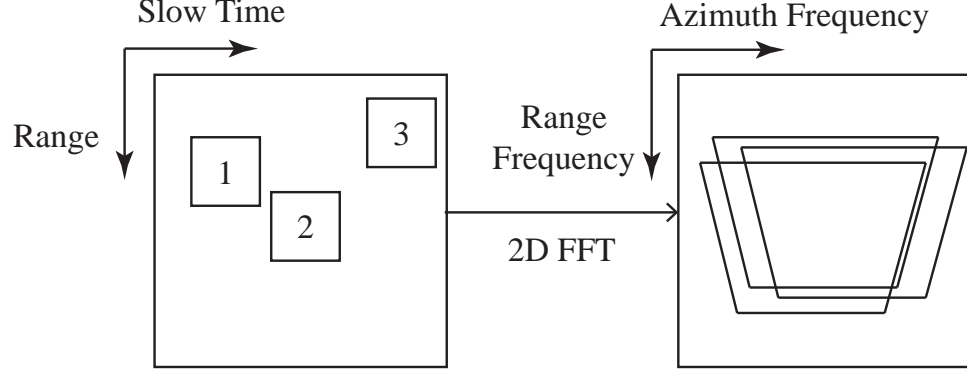Figure 6.1. The processing steps of Phase Gradient Algorithm

Figure 6.2. Illustration of spectrum mis-alignment

an object right in front of the radar antenna will experience most phase error, and an object at an angle to the left or right will experience less phase error.

6.3   Design Considerations for the Modified PGA

In the previous section, we have discussed the signal processing chain of the conventional PGA, as well as some of its limitations. The conventional PGA has quite limited in what case it can be applied. To be precise, it assumes the input signal is taken in spotlight configuration, the image is focused using frequency domain algorithms, and the geometry is for far range such that the phase error of all range bins at a particular pulse pair would be the same theoretically. These limitations has posed a stop sign of using PGA in our system, where it is in stripmap configuration, focused using Fast Backprojection method, and works very close to the ground with range starting at nearly zero.

To fix this issues, some modifications are done to the signal processing chain to make PGA compatible with our signal model and system design. Some of these modifications are just adding an extra layer to interface between different signal model assumptions.

6.3.1 Assumptions

We assume the followings in the modified PGA:

- The input to the signal processing chain is a 2D matrix of pre-focused image taken in stripmap SAR configuration.

- The image was pre-focused using Fast Backprojection method.

- The imaging area is from range zero to some range R, and azimuth from one end of the trajectory to the other end of the trajectory.

6.3.2 Spotlight and Stripmap

The issue of conversion between spotlight and stripmap is the easiest-to-solve among the 3. The characteristics of range profiles collected with spotlight configuration is the matched-filter is designed in a way such that all the raw received signal is filtered with reference to the scene center. Hence there is no range cell migration in the ROI (assuming it is small), and the phase in the range profile is relative to that of the scene center. In addition, the target is visible over the whole aperture. Stripmap on the other hand has a azimuth independent matched-filtering, hence there is range cell migration and the phase reference is often set to a constant range in the range profile rather than constant range in the image grid. Also, the target may not be visible over the whole aperture. With these in mind, the conversion can be done by performing RCMC, followed by offsetting the phase of each range profile, and lastly windowing along azimuth to remove any targets that do not span the full aperture.

Alternatively, one can start from a pre-focused image. Assume we have a pre-focused image as an input, an azimuth Fourier transform of the input image should yield the range profiles equivalent to that collected in spotlight mode. This approach greatly reduce the complexity, all it need is a pre-focused image with some blur. The drawback being that if the defocus is too severe or if there is some strong range error

such that a single target split into two in range, the algorithm will not be able to correct the defocusing.

6.3.3 Frequency and Time domain algorithm

One major difference between the two types of algorithms is that frequency domain focusing algorithms focus the image in one common kernel, while time domain focusing algorithms focus each pixel with a separate kernel. As a result, the spectrum of each region of the focused image do not align with each other. To fix this, we perform spectrum alignment to the input image. It can be think as the time domain algorithm is "too-exact" in modeling the phase of each of the pixels, and spectrum alignment is an extra step to "re-add" the previously removed extra phase.

The spectrum alignment [31] is a step to add phase to each of the pixel. To begin with, one has to define a scene center, and compute the range from the scene center to each of the pixels. The phase correction applied to each pixel has the form:

$$\phi_i = exp(j\frac{4\pi}{\lambda}R_i) \tag{6.10}$$

where R_i is the range from reference scene center to pixel i.

6.3.4 Far Range and Near Range

The problem with near range and wide ROI can be thought as having targets that are widely spread in a large range of angle of arrival. In the high-altitude SAR situation, since the beam is narrow, and there is return signal for every range due to the elevation angle, the azimuth phase error vector of each range bins should converge to a common error vector. However, in the large ROI case, refer to figure 6.3, targets at different range bins can experience very different phase error depending on the instantaneous relative position of the target relative to the radar antenna. Also when the Radar system is traveling very close to the ground, the elevation angle is very

small, hence some of the range bins simply do not have a meaningful amplitude response. The phase of those low amplitude bins should not be taken into account when estimating the phase error.

To solve this issue, the author proposed a motion modeling method to the PGA, which models the phase error as a function of azimuth and range motion error, and applies a different phase correction to each range bins instead of a bulk correction of the average error.
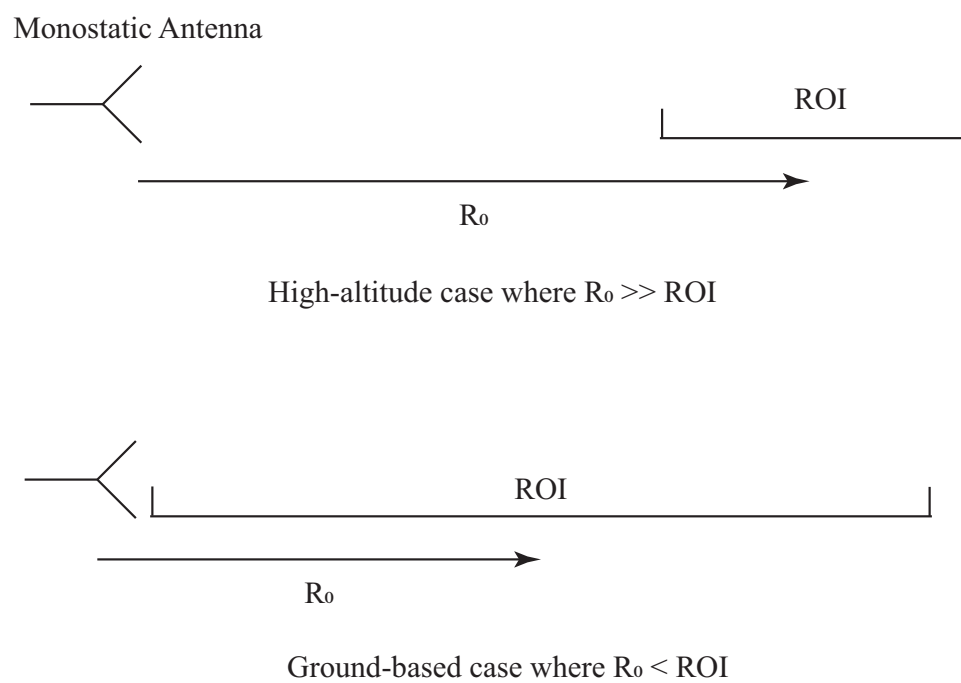
Monostatic Antenna

ROI

R_0

High-altitude case where $R_0 \gg$ ROI

ROI

R_0

Ground-based case where $R_0 <$ ROI

Figure 6.3. Illustration of geometry in high-altitude SAR vs ground-based SAR

6.4   Motion modeling

The idea of motion modeling is to find a common basis of the phase error in the array of range bins. We consider a 2D motion model, where the Radar is pointing in range direction, and moving in azimuth which is perpendicular to the range. The motion errors are expressed in deltas in range and azimuth axis, as shown in figure 6.4.
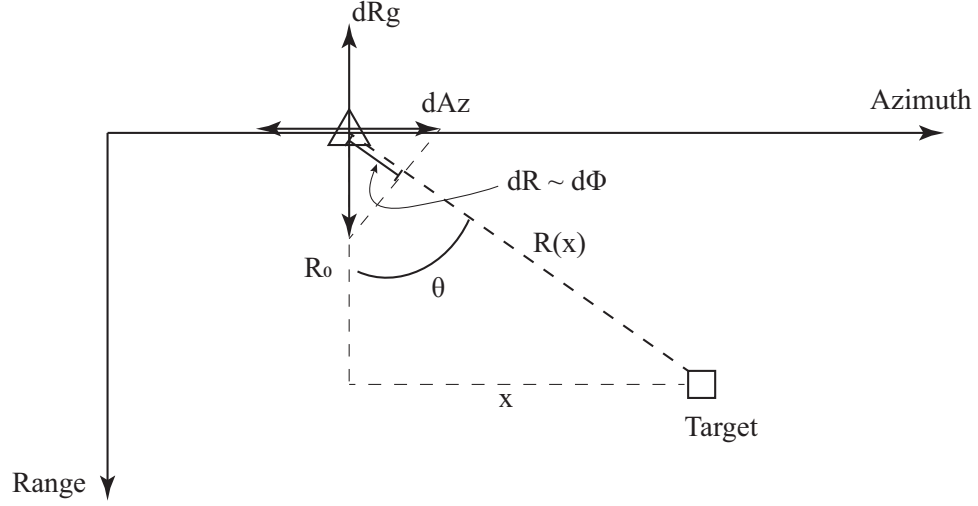
Figure 6.4. Motion error modeling of Modified PGA

Now, consider a target located at (Range, Azimuth) = (R_0, x) relative to the instantaneous radar antenna position at a certain pulse index, the phase of the range profile at the range $R(x) = \sqrt{R_0^2 + x^2}$ should be proportional to $exp(j4\pi/\lambda * R(x))$ if the relative position between radar and target is exact.

The error in radar position is expressed in dRg and dAz as labeled in the figure, and the resultant delta range $dR = \sqrt{dRg^2 + dAz^2}$ is directly proportional to the error in phase.

We observed that the proportionality between dRg and dAz to the phase error is actually a function of angle of arrival (AOA), θ. Hence we can compute the basis of

the phase error in terms of dRg and dAz, and apply the phase error based on the AOA of dominant target at each range bin.

6.5   The Signal Processing Steps

Integrating the above modifications to the PGA, the signal processing steps is outlined as follow:

- Prefocus the image

- Spectrum Alignment

- Estimate AOA

- Circular Shift and Windowing

- Mask range bins

- Compute phase error per range

- Solve for dRg and dAz

- Refine error estimation, apply correction and iterate

Prefocus the image

The input to the algorithm is assumed to be a prefocused image of size (M, N). The image may not be perfectly focused such that some blurs exist. The image is assumed to be focused using Fast Backprojection algorithm.

Spectrum Alignment

A phase correction is applied to the input image according to equation (5.1), which serve the purpose of spectrum alignment. The amplitude of the input image should not be changed, however, the phase multiplication will alter the spectrum of the image. The 2D FFT of any sub-region of the image after multiplying the phase correction should align perfectly. Note that this step is not needed if the input image is focused using frequency domain method like the Omega-K algorithm.

Estimate AOA

The AOA can be estimated in multiple ways. If the radar has MIMO transceiver, the AOA can be estimated from the phase difference between receiving antennas of known baseline. This method is used and will be discussed in chapter 7.

The other method is taking advantage of the prefocused image. Since the input image is prefocused, the position of each targets are approximately known. One can locate the target for each range bin by taking argmax of the amplitude, and by simple geometry, compute the angle of arrival θ as an array for each range bins.

The estimated AOA is a 2D array of size (M, N).

Circular Shift and Windowing

The circular shift and windowing are similar to that of the original PGA.

Mask range bins

Masking the range bins is essential for SAR operating at a very small elevation angle close to the ground. In aerial platform, the SAR system is often designed to scan at an elevation angle to the ground such that there is some form of targets at every range bins in the ROI.

The phase of the signal in a particular range bin is the summation of the complex returns (can be thought as a vector) of all the targets within that bin, plus system noise.

For ground-based systems, not all range bins of the return signal has some significant targets, in the extreme case, a large number of range bins can be totally 'clean' and return a very low amplitude. Under these circumstances, the phase of those range bins will be dominated by noise and very often the direct coupling between TX and RX antennas, which means it will be very wrong to estimate the phase error using those range bins.

By applying a mask to the range bins, and remove those with low or insignificant amplitude response, the estimation accuracy for the phase error in bins where there is an actual target is greatly enhanced.

Compute the phase error per range

This step is similar the original PGA with the exception it only performs the operation in equation (6.6) and (6.7), not proceeding to the averaging step in (6.8).

The phase error per range is an array of length N, with first element being zero.

Solve for dRg and dAz

According to the geometry in figure 6.4, we can write the relation of phase and motion error as follow:

$$\delta\phi_e(k) = \frac{4\pi}{\lambda}(dRg(k) \cdot cos(\theta_k) + dAz(k) \cdot sin(\theta_k)) \qquad (6.11)$$

where k is the azimuth pulse index; $\delta\phi_e(k)$ is the phase error array of length M for pulse k; dRg and dAz is the motion error for pulse k; $cos(\theta_k)$ and $sin(\theta_k)$ is an array of length M.

We solve the over-determined equation (6.11) by rewriting it in matrix form:

$$\begin{bmatrix} \delta\phi_e(k) \\ \vdots \end{bmatrix} = \frac{4\pi}{\lambda} \begin{bmatrix} cos(\theta_k) & sin(\theta_k) \\ \vdots & \vdots \end{bmatrix} \begin{bmatrix} dRg \\ dAz \end{bmatrix} \qquad (6.12)$$

Using the Least Square Estimator, the solution is:

$$\begin{bmatrix} dRg \\ dAz \end{bmatrix} = \frac{\lambda}{4\pi}[A^T A]^{-1} A^T y \qquad (6.13)$$

where

$$A = \begin{bmatrix} cos(\theta_k) & sin(\theta_k) \\ \vdots & \vdots \end{bmatrix} \qquad (6.14)$$

$$y = \begin{bmatrix} \delta\phi_e(k) \\ \vdots \end{bmatrix} \qquad (6.15)$$

Refine error estimation, apply correction and iterate

After knowing the error basis dRg and dAz, we recompute the phase error for each range bins using equation (6.11), and the correction is applied to the Fourier transform of the input image. The process is repeated until the image focusing quality is improved.

6.6   Testing the Algorithm

The modified PGA is tested with real data collected on a ground-based SAR system with some motion error introduced. The output image was compared with that processed by the original PGA, and it has been shown to perform much better than the original PGA in the experiment setup.

6.6.1   Experiment Setup

The experiment was conducted on a custom SAR system based on the IWR1443 radar solution by Texas Instrument [14]. The radar signal model can be described as in equation (2.22). The radar was installed on a linear positioning platform of length 1 meter powered by a stepper motor, and the dimension of the room was about 6 meters by 4 meters. The dimension of imaging area was 12 meters by 1 meter. 4 custom stationary corner reflectors are deployed in the room, which the approximate position is labeled in figure 6.5 in the format of (azimuth, range).

In figure 6.5, the radar moves along an aperture of 1 meter at the left side, pointing to the right. The maximum range was computed to be approximately 12.1 meters, hence the imaging area is longer then the room, such that the wall and some reflection is expected to be observed. To reduce complexity of the problem, a range mask was applied such that bins beyond 6 meters range was not considered when computing the phase correction using PGA.

6.6.2   Result and Analysis

A SAR acquisition was performed using the geometry and setup mentioned above, with some perturbation in the track, and the image is pre-focused using the Fast Backprojection algorithm outlined in section 3.2.1. The log-amplitude of the input image is shown in figure 6.6, where a blurring is observed across azimuth, especially

for corner reflectors at (0.6, 3) and (0.1 ,4). Note the axis label of the images are in pixels.

The stock PGA and the modified PGA was used to improve the image focus. The result has shown a great improvement of using the modified PGA versus the stock PGA in improving the focusing of the image, in terms of sharpness of the corner reflectors being placed around the imaging area.

Figure 6.7 and 6.8 shows the improved image processed by the stock PGA and modified PGA respectively with an iteration of 10 steps.

Improvement by modeling the motion

The image processed by the stock PGA shows little sign of improvement, and is even worse in some areas. The reason is because stock PGA assumes every pixels to be in far range, and estimate the phase error using an averaging operation. In out setup, this assumption cannot hold, and the instantaneous phase error at a certain azimuth pulse for the range bin where the target is to the left can be very different from that for a target to the right. By computing the average, the estimated phase error is not close to either targets, hence it is unable to improve the focus quality. On the other hand, the modified PGA model the phase error by taking the information of where the target is located, and apply a differential correction to each of the range bins, hence the estimation is more accurate, with observable sharpening according to result in figure 6.8.

Convergence

The intermediate images of the modified PGA is shown in figure 6.9. Where we can observe an acceptable convergence at around iteration 3. It has to be noted that the rate of convergence is dependent on the target profile and the quality of the pre-focused input image, that is, we cannot draw a general conclusion of the performance of PGA in terms of the processing speed.

6.7   Limitations

While being a powerful tool to improve the sharpness of SAR image, PGA has some limitations, including the offline-processing requirement, unable of sharpening when there is severe RCM, and requiring the input of a pre-focused image.

The offline-processing requirement is mainly a result of iterative-nature. As discussed before, PGA is an iterative algorithm that improve the phase error estimation based on the previous iteration of sharpened image. This processing is very slow, and require a whole aperture to be processed at once. For most of the SAR systems that performs real-time image, PGA is not acceptable in the sense that it takes too long to iterate, and it prevented the signal processing chain to update at a faster rate by taking incremental pulse update.

The RCM problem arise when the error of track used to generate the pre-focused input image is too bad such that it exceed a range resolution cell. Usually that happen when there is a jump in the track, which cause different part of the aperture to observe the target at a different pixel in the image domain. Since the signal model of the input image assumed by PGA is just a phase function along azimuth, any range migration problem that cause a target to split into 2 or more in range is not corrected by PGA.

Given the above intrinsic limitations of the PGA, the author has proposed a novel method to improve the focusing of SAR, called the MPGA. Under the MPGA framework, together with the use of time domain focusing algorithms, the SAR signal processing chain is a pulse-by-pulse process with real-time capability. In addition, it is not limited to azimuth sharpening as we do not assume an azimuth signal model while using time domain algorithms.
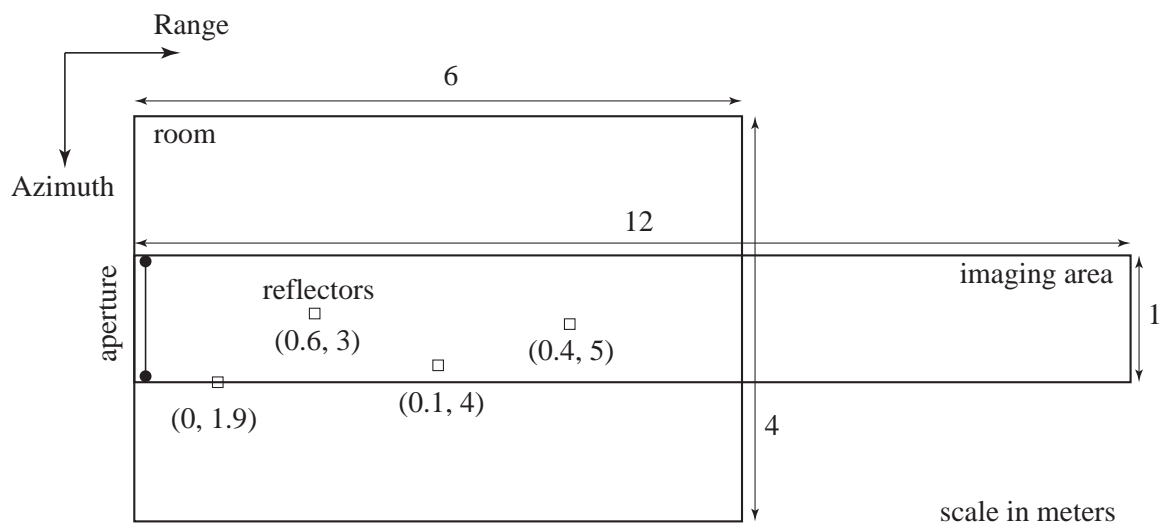
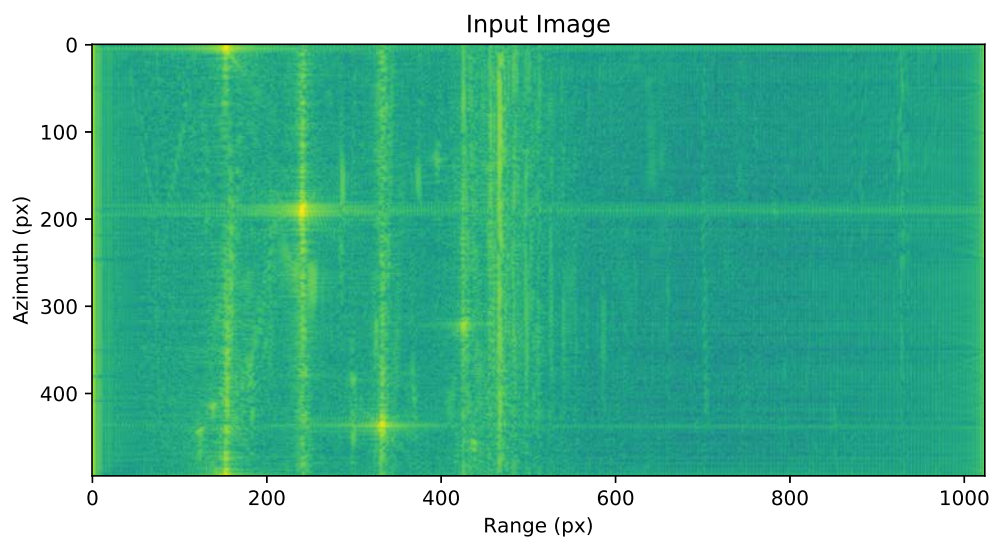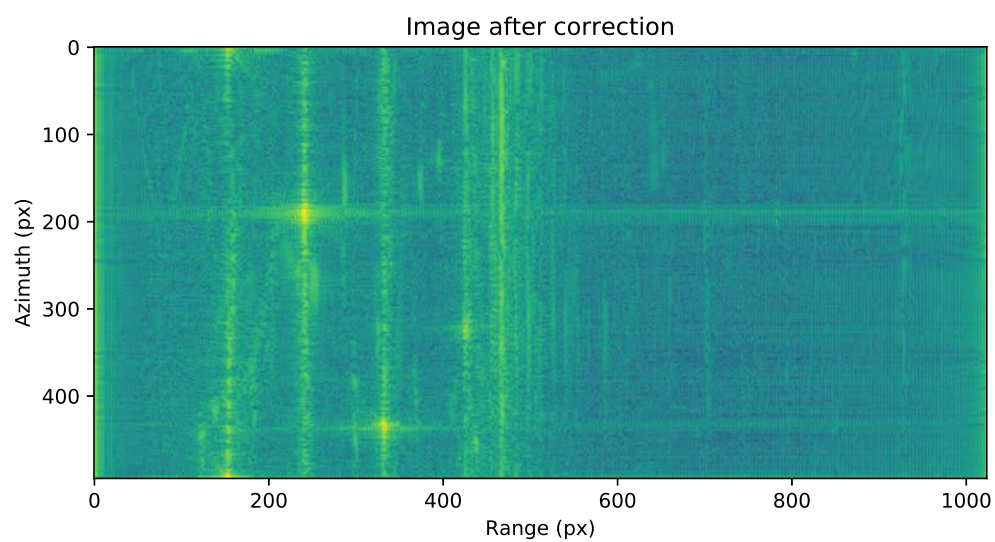Figure 6.5. Experiment setup for testing the Modified PGA

Figure 6.6. Input pre-focused image to PGA
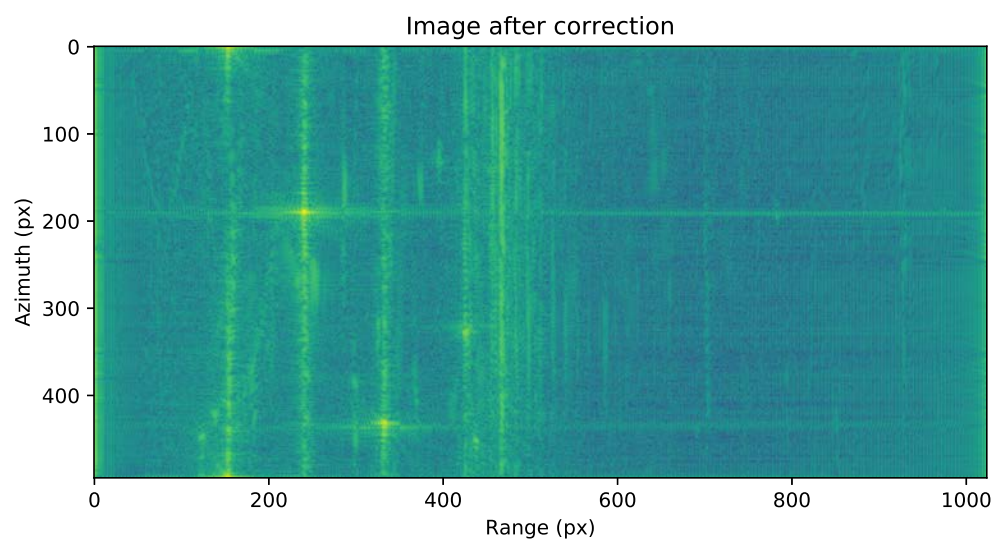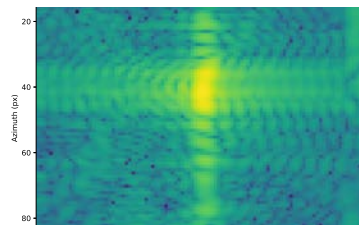
Figure 6.7. Improved image processed by stock PGA
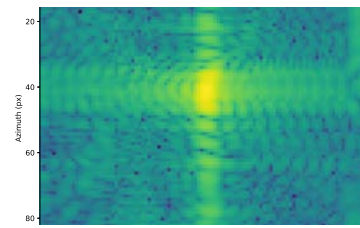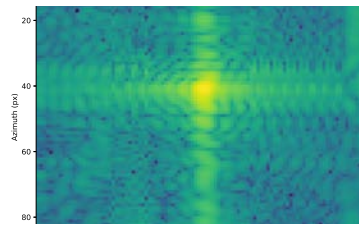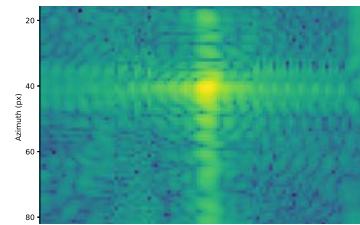

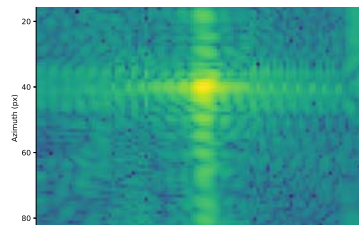Figure 6.8. Improved image processed by modified PGA
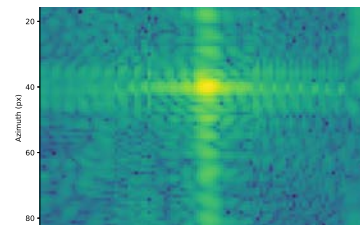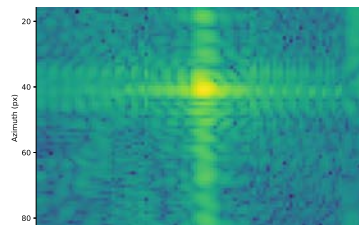
(a) iteration 1

(b) iteration 2
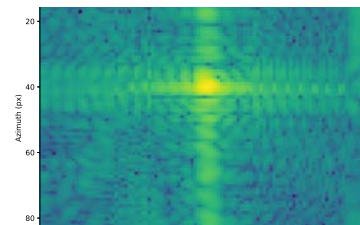
(c) iteration 3

(d) iteration 4

(e) iteration 5

(f) iteration 6

(g) iteration 7

(h) iteration 8

Figure 6.9. Intermediate images of the modified PGA centered at target (0.6, 3)

7. THE MPGA

7.1 Background

7.1.1 Problems and Challenges

SAR systems relies heavily on accurate timing and positioning. These 2 pieces of information is essential for reconstructing the synthetic array of antennas, and any small error on the order of one-tenth of wavelength in the position can severely impact the quality of the SAR image.

Conventional SAR systems often employs the GNSS/INS positoning solutions [10] [11] [16] [21], which use a constellation of satellites to provide global absolute positioning and timing at a slower rate (often 5Hz), and an integration of accelerometer, magnetometer, and gyroscope to "fill the gap" at a higher rate (hundreds Hz). While this solution is good for high-altitude SAR where GNSS reception is excellent and trajectory is close to linear over the aperture length, it is hardly reliable for Radar platforms traveling near the ground.

7.1.2 Solution

MPGA, stands for MIMO Phase Gradient Algorithm, is a novel algorithm invented by the author which aims to provide a motion estimation solution for Multiple-Input-Multiple-Output (MIMO) Radar systems using the Radar return signal. Although it is named with Phase Gradient Algorithm, it has very minimal relation with the original PGA logic, however, the part of estimating the phase gradient in the original PGA using iterative logic is replaced when we have MIMO configuration.

MPGA has advantages over conventional positioning solutions in the following aspects:

Availability In contrast to GNSS/INS solution, MPGA does not depend on satellite coverage, hence the position information is always available no matter the system is traveling in the city, under the bridge, or inside a tunnel. The only dependence of MGPA is the radar return signal, that is, something has to be in the scene and be illuminated by the Radar beam, if nothing is present, obviously no changes can be observed in the return signal and the position cannot be computed.

Timing and Updating Frequency The position of the Radar is computed from the MIMO return signal. To be precise, the deltas of the Radar pose is computed given any pair of pulse. This is very different compared to conventional way of positioning, which uses a separate sensor with a separate clock / oscillator, and a separate updating frequency. Those sensors have to output the position along with a timestamp, which not only requires an extra step to interpolate the positions to the Radar pulse rate, but also bringing up some synchronization problem since the GNSS/INS clock is often not the same as Radar ADC clock.

MPGA, on the other hand, totally eliminated this problem because the position is computed exactly per pulse pair, hence no time-stamping is needed. The x-axis is simply pulse, instead of time. Given a SAR system which has a PRF of more 1 - 10kHz, MPGA can provide the native updating rate, while GNSS/INS can only rely on interpolation to up-sample the positioning information.

System Complexity and Redundancy Positioning with the GNSS/INS system requires every components including the Radar antenna(s), GPS antenna(s), INS unit to be mounted on a rigid frame with precisely measured extrinsic. The extrinsic is often hard-coded into the system and requires update over a period or everytime when the system is reinstalled.

The MPGA system do not take multiple sensor reading - everything is computed from the MIMO Radar return signal. The position computed by MPGA is the exact position of the antenna electrical phase center. This prevents any calibration error when measuring Radar extrinsic, and reduced the step of applying translations and rotations from the sensor frame to the Radar antenna frame.

7.2 Simplified version

To better illustrate how MPGA works, we consider a simplified version, shown in figure 6.1, where there is a Radar system having one TX and two RX, moving in a perfectly linear trajectory along Azimuth, and facing broadside in a stripmap configuration. The TX and RX antennas are located such that they are all collinear along azimuth. We label the RX antennas to be RxA and RxB, the baseline between 2 RX being B_n, the phase measured by antenna X at position Y being ϕ_{XY}, and the distance traveled by the Radar along azimuth between 2 pulses (or chirps) being dx. We also consider a single target located at arbitrary position (R_0, x_0) within the beam illumination.

The curved line (not to scale) in figure 7.1 illustrate the hyperbolic phase of the target when observed at different positions by the Radar along azimuth. For simplicity we assume there is no range migration or phase wrapping within the 2 pulses being measured.

For a small azimuth motion, it is straight forward to establish a linear relation between the distance traveled dx and the phase changed $d\phi$ according to the figure 7.1:

$$dx = \frac{B_n}{d\phi_{A1B1}} d\phi_{A1A2} \tag{7.1}$$

where $d\phi A1B1$ is the phase difference between RxA and RxB at position 1; $d\phi_{A1A2}$ is the phase difference between RxA at position 1 and RxA at position 2.

Since there should not be range cell migration for successive azimuth chirps, we can estimate dx between each chirp pairs, and integrate dx to obtain the track along azimuth direction. Note that range is assumed to be error-less in this simplified version.

7.3 Generalized version for 1D baseline

We generalize MPGA from the simplified version. By generalization, the algorithm can take arbitrary number of RX antennas, and output the track in both azimuth and range direction motion, together with heading of the radar platform.

7.3.1 Assumptions

The following are assumptions taken when deriving the generalized MPGA for 1D baseline:

- The radar is only moving on a 2D plane.

- The antenna spacing (baseline B) do not exceed the azimuth Nyquist sampling requirement, such that

$$\sqrt{dAz^2 + dRg^2} \leq B < N \tag{7.2}$$

  where dAz and dRg are the motion of radar in between 2 chirps along azimuth and range direction respectively; B is the baseline; N is the Nyquist sampling requirement calculated from equation (2.29) and (2.40).

- The antennas are equally spaced.

- Targets are stationary.

- Radar is nearly stationary within the duration of a chirp (stop-and-go approximation).

- More than 2 point targets is illuminated by the beam at any given pulse pair.

7.3.2 The Geometry

The geometry of the following discussion is based on Figure 7.2 and 7.3. Consider an array of 4 receive antennas, equally spaced by Bn constrained by the assumption
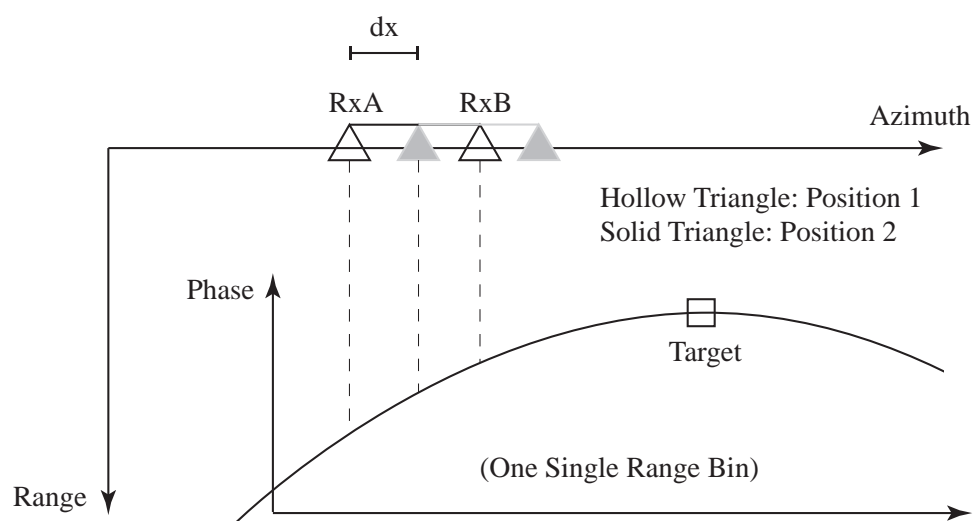
Figure 7.1. Geometry of the simplified version of MPGA

in equation (7.2). We label the antenna to be 0, 1, 2, 3 from left to right. If we consider computing the target angle-of-arrival (AOA) using any 2 of the antennas, pair (0, 1) will be able to resolve a target located in region A, B, and C; pair (0, 2) will be able to resolve a target in region A, B; pair (0, 3) will only be able to resolve region A. The region A, B and C are called the target regions, which the boundary is determined by the aliasing of phase when solving the AOA using a large baseline:

$$\theta = sin^{-1}(\frac{d\phi\lambda}{4\pi B}) \tag{7.3}$$

where θ is the angle between a line on the 2D plane of radar motion perpendicular to the receiver array and the boundary between target regions (dotted line in figure 7.2); B is the separation between any 2 receive antennas.

The motion of the radar can be divided into sub-regions of I, II, and III, which is defined as the multiple of the length of the shortest receiver baseline.

Next, we consider there are 3 degrees of freedom in the motion of the Radar platform, which are motion in azimuth, motion in range, and change in heading. For instance, if there are one TX and 2RX as drawn in figure 6.3, and the antenna array moved from position 1 to position 2, the motion of each antenna i is labeled as dR_i and dx_i, and the change in heading is labeled as Φ. By simple geometry, we know the following:

$$dR_2 = dR_1 - B_R sin(\Phi) \tag{7.4}$$

$$dx_2 = dx_1 - B_R(1 - cos(\Phi)) \tag{7.5}$$

$$dR_3 = dR_1 - B_T sin(\Phi) \tag{7.6}$$

$$dx_3 = dx_1 - B_T(1 - cos(\Phi)) \tag{7.7}$$

Our goal is to solve for dR_1, dx_1 and Φ per pulse pair, and integrate them to obtain the track of the radar platform.
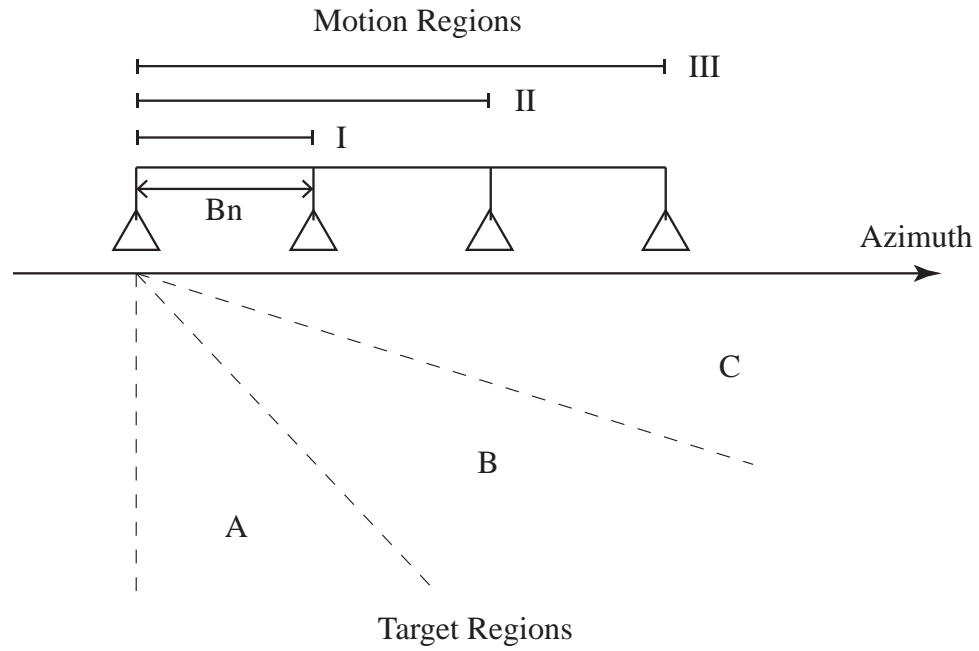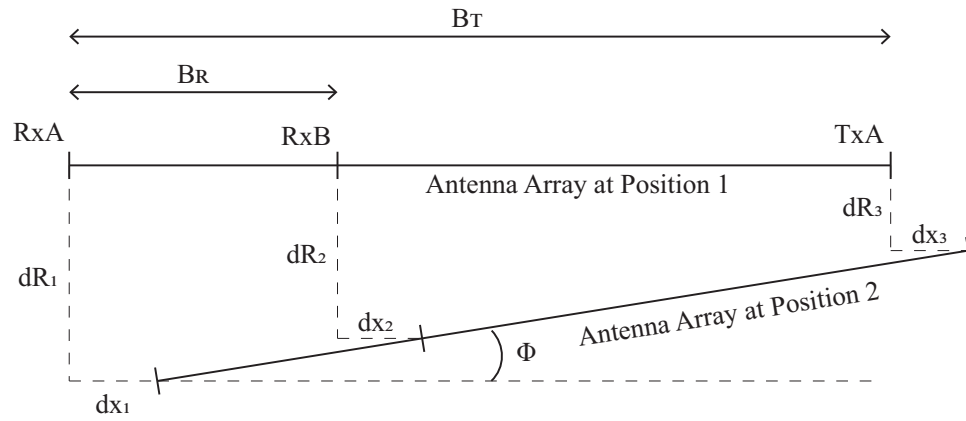
Figure 7.2. Geometry of the generalized MPGA

Figure 7.3. Geometry of the generalized MPGA

7.3.3 Target Identification

MPGA computes the motion of the Radar platform by observing how the targets move between pulses. In order to observe the target, the first step is to identify where the target is, more explicitly, the index of the range bins where there are useful targets.

This problem is similar to the modified PGA where we have to select a number of range bins which have actual signal returns in the range profile, because in the ground-based geometry, it is possible for some range bins having very low amplitude, and the phase of those bins do not store meaningful information. The CFAR algorithm is used to identify useful range bins.

A Cell-Averaging CFAR [25] [26] is used to identify useful range bins. For each range bins in the range profile, labeled as Cell-Under-Test (CUT) in figure 7.4, a window of guard cells and training cells are created. Guard cells are the neighboring range bins which are not contributed to the computation of the background esti-mation, and training cells are the range bins beyond guard cells which are used to estimate the background for CUT.

Given the constant false alarm α, the threshold for the simple hypothesis testing is

$$T = \alpha^{-1/N} - 1 \tag{7.8}$$

where T is the threshold; N is the number of training cells.

A boolean mask is given to each of the range profile for every chirps acquired along the synthetic aperture, where False is given when the CUT has amplitude smaller than threshold, and True for CUT bigger than threshold. After target selection, the data is presented in a variable length array, where the length is the number of range bins selected, and is different for every azimuth pulse.
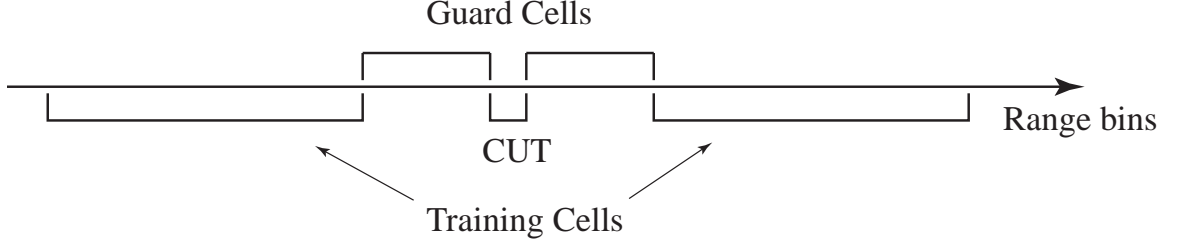
Figure 7.4. The cell labeling in CFAR algorithm

7.3.4   Motion Estimation

After identifying the index of useful range bins, consider a radar with 4 receive antennas, the range profile will be of dimension (4 channels x selected range bins) for every azimuth pulse. The phase difference is computed across each receive antennas in one radar position, and also across receive antennas between a pair of radar position [33].

We denote the phase difference between antenna X and Y in position i and j to be $d\phi_{XiYj}$, such that for the 4 antenna case, we have a tensor of 4 x 4 x range bins for the phase difference $d\phi_{11}$ within one radar pulse, and another tensor of same size for the phase difference $d\phi_{12}$ between 2 pulses. The first 2 dimension of the tensors are given as the following matrix:

$$d\phi_{11} = \begin{bmatrix} d\phi_{A1A1} & d\phi_{B1A1} & d\phi_{C1A1} & d\phi_{D1A1} \\ d\phi_{A1B1} & d\phi_{B1B1} & d\phi_{C1B1} & d\phi_{D1B1} \\ d\phi_{A1C1} & d\phi_{B1C1} & d\phi_{C1C1} & d\phi_{D1C1} \\ d\phi_{A1D1} & d\phi_{B1D1} & d\phi_{C1D1} & d\phi_{D1D1} \end{bmatrix} \tag{7.9}$$

$$d\phi_{12} = \begin{bmatrix} d\phi_{A1A2} & d\phi_{B1A2} & d\phi_{C1A2} & d\phi_{D1A2} \\ d\phi_{A1B2} & d\phi_{B1B2} & d\phi_{C1B2} & d\phi_{D1B2} \\ d\phi_{A1C2} & d\phi_{B1C2} & d\phi_{C1C2} & d\phi_{D1C2} \\ d\phi_{A1D2} & d\phi_{B1D2} & d\phi_{C1D2} & d\phi_{D1D2} \end{bmatrix} \tag{7.10}$$

	C	B	A
I	$\begin{bmatrix} 0 & 1 & 2 & 3 \\ -1 & 0 & 1 & 2 \\ -2 & -1 & 0 & 1 \\ -3 & -2 & -1 & 0 \end{bmatrix}$	$\begin{bmatrix} 0 & 0 & 1 & 2 \\ 0 & 0 & 0 & 1 \\ -1 & 0 & 0 & 0 \\ -2 & -1 & 0 & 0 \end{bmatrix}$	$\begin{bmatrix} 0 & 0 & 0 & 1 \\ 0 & 0 & 0 & 0 \\ 0 & 0 & 0 & 0 \\ -1 & 0 & 0 & 0 \end{bmatrix}$
II	$\begin{bmatrix} -1 & 0 & 1 & 2 \\ -2 & -1 & 0 & 1 \\ -3 & -2 & -1 & 0 \\ -4 & -3 & -2 & -1 \end{bmatrix}$	$\begin{bmatrix} 0 & 0 & 1 & 2 \\ -1 & 0 & 0 & 1 \\ -2 & -1 & 0 & 0 \\ -3 & -2 & -1 & 0 \end{bmatrix}$	$\begin{bmatrix} 0 & 0 & 0 & 0 \\ 0 & 0 & 0 & 0 \\ -1 & 0 & 0 & 0 \\ -2 & -1 & 0 & 0 \end{bmatrix}$
III	$\begin{bmatrix} -2 & -1 & 0 & 1 \\ -3 & -2 & -1 & 0 \\ -4 & -3 & -2 & -1 \\ -5 & -4 & -3 & -2 \end{bmatrix}$	$\begin{bmatrix} -1 & 0 & 0 & 0 \\ -2 & -1 & 0 & 0 \\ -3 & -2 & -1 & 0 \\ -4 & -3 & -2 & -1 \end{bmatrix}$	$\begin{bmatrix} 0 & 0 & 0 & 0 \\ -1 & 0 & 0 & 0 \\ -2 & -1 & 0 & 0 \\ -3 & -2 & -1 & 0 \end{bmatrix}$

A correction matrix was computed to correct for the phase wrapping of antenna pairs having baseline longer than the Nyquist requirement using the AOA information provided by the shortest baseline. The correction matrix has dimension of 4 x 4 in this case, and formulated such that

$$d\phi_{wrapped} = d\phi_{true} + correction * \pi \qquad (7.11)$$

The correction matrix is given in the following table according to the motion region and target region:

After the phase is being corrected, refer to figure 7.3 and consider a target located at arbitrary location (x, R). The path difference traveled by the signal from TX to each of the RX can be calculated as follow for the 2 antennas in the figure:

$$AA \quad AB \quad AC \quad AD$$
$$BA \quad BB \quad BC \quad BD$$
$$CA \quad CB \quad CC \quad CD$$
$$DA \quad DB \quad DC \quad DD$$

$$dR_{A1B1} = dR_{A1} + dR_{C1} - dR_{B1} - dR_{C1} \tag{7.12}$$

$$\approx B_R sin\theta \tag{7.13}$$

$$dR_{A1A2} = dR_{A1} + dR_{C1} - dR_{A2} - dR_{C2} \tag{7.14}$$

$$= \sqrt{x^2 + R^2} + \sqrt{(x - B_T)^2 + R^2} - \sqrt{(x - dx)^2 + (R - dR)^2} \tag{7.15}$$

$$- \sqrt{(x - dx + B_T(1 - cos\Phi) - B_T)^2 + (R - dR + B_T sin\Phi)^2} \tag{7.16}$$

$$\approx sin\theta(2dx + B_T(cos\Phi - 1)) + cos\theta(2dR - B_T sin\Phi) \tag{7.17}$$

where dR_{Xi} is the range from antenna X at position i to the stationary target; θ is the angle of arrival to the target.

dR_{XiYj} is related to $d\phi_{XiYj}$ by

$$d\phi_{XiYj} = \frac{2\pi}{\lambda} dR_{XiYj} \tag{7.18}$$

By using the phase difference in tensor $d\phi_{11}$, we can obtain the angle-of-arrival for each of the range bin and azimuth pulse. With equation (7.18), we substitute the AOA into equation (7.17) to obtain dx, dR, and Φ.

For a 4 antenna (A, B, C, D) configuration, we consider a matrix notation that denote the quantities corresponding to the specific antenna pair having the form:

Equation (7.17) can be generalized into a matrix form for all antenna pairs:

$$d\phi_{ij} = \frac{2\pi}{\lambda}(sin\theta c_{ij} + cos\theta m_{ij}) \tag{7.19}$$

where

$$c_{ij} = 2dx + k_{1ij}cos\Phi + k_{2ij} \tag{7.20}$$

$$m_{ij} = 2dR + k_{3ij}sin\Phi \tag{7.21}$$

and

$$k_{1ij} = \begin{bmatrix} B_T & B_T + B_{R1} & B_T + B_{R2} & B_T + B_{R3} \\ B_T & B_T + B_{R1} & B_T + B_{R2} & B_T + B_{R3} \\ B_T & B_T + B_{R1} & B_T + B_{R2} & B_T + B_{R3} \\ B_T & B_T + B_{R1} & B_T + B_{R2} & B_T + B_{R3} \end{bmatrix} \qquad (7.22)$$

$$k_{2ij} = \begin{bmatrix} -B_T & -B_T & -B_T & -B_T \\ -B_T - B_{R1} & -B_T - B_{R1} & -B_T - B_{R1} & -B_T - B_{R1} \\ -B_T - B_{R2} & -B_T - B_{R2} & -B_T - B_{R2} & -B_T - B_{R2} \\ -B_T - B_{R3} & -B_T - B_{R3} & -B_T - B_{R3} & -B_T - B_{R3} \end{bmatrix} \qquad (7.23)$$

$$k_{3ij} = \begin{bmatrix} -B_T & -B_T - B_{R1} & -B_T - B_{R2} & -B_T - B_{R3} \\ -B_T & -B_T - B_{R1} & -B_T - B_{R2} & -B_T - B_{R3} \\ -B_T & -B_T - B_{R1} & -B_T - B_{R2} & -B_T - B_{R3} \\ -B_T & -B_T - B_{R1} & -B_T - B_{R2} & -B_T - B_{R3} \end{bmatrix} \qquad (7.24)$$

$$(7.25)$$

B_T, B_{R1}, B_{R2}, B_{R3} are baselines of TX, RxB, RxC, RxD relative to RxA respectively.

Equation (7.19) is over-determined, and is solved in 2 separate step using the lease square method. In the first least square, c_{ij} and m_{ij} are being computed from $d\phi_{ij}$ for each of the available range bins in that azimuth pulse. In the second least square, dx, dR, and Φ are being computed from c_{ij} and m_{ij}.

7.3.5   Near Field Correction

The mathematical model described in equation (7.19) used an approximation in estimating the angle-of-arrival θ, which is appropriate only for far-field targets. A correction is required for targets located in the near field.

Consider the 2D Cartesian plane where the radar moves, and a target located at arbitrary position of the plane. The AOA is the angle between the normal of the Radar antenna array and the line joining the target and the center of array, hence, if

one draw the line of constant AOA on the 2D plane, the lines should be linear and intersecting the center of the array.

However, while estimating the AOA using phase difference across the antenna array with known baseline, the line of constant phase difference is given by a hyperbola, as shown in figure 7.5. Consequently, the one-to-one mapping of AOA with phase difference cause the line of constant AOA to be a hyperbola too. The error between true AOA and the AOA estimated from phase difference is the difference between θ_1 and θ_2 in figure 7.6.

The problem can be reduced by adding a correction term to the basis in equations in the first least square estimation. For instance, we consider the derivation of equation (7.17):

$$dR_{A1A2} = dR_{A1} + dR_{C1} - dR_{A2} - dR_{C2} \tag{7.26}$$

$$= \sqrt{x^2 + R^2} + \sqrt{(x - B_T)^2 + R^2} - \sqrt{(x - dx)^2 + (R - dR)^2} \tag{7.27}$$

Expanding (7.27) yields:

$$dR_{A1A2} \approx dx \frac{x}{\sqrt{x^2 + R^2}} + dR \frac{R}{\sqrt{x^2 + R^2}} \tag{7.28}$$

$$+ dx \frac{x - B_T}{\sqrt{(x - B_T)^2 + R^2}} - \sqrt{(x - B_T)^2 + R^2} \tag{7.29}$$

$$- B_T(1 - cos\Phi) \frac{x - B_T}{\sqrt{(x - B_T)^2 + R^2}} + dR \frac{R}{\sqrt{x^2 + R^2}} \tag{7.30}$$

$$- B_T sin\phi \frac{R}{\sqrt{x^2 + R^2}} \tag{7.31}$$

Consider the fraction in the 5th term:

$$\frac{x - B_T}{\sqrt{(x - B_T)^2 + R^2}} \approx \frac{x - B_T}{\sqrt{x^2 + R^2}} \tag{7.32}$$

$$\approx sin\theta - \frac{B_T}{Range} \tag{7.33}$$

where $Range$ is the distance from antenna to the target range bin.

Hence, the correction is applied by changing the basis in the first least square estimation from $(sin\theta,\ cos\theta)$ to $(sin\theta - \frac{B}{Range},\ cos\theta)$, where B is the baseline between the 2 antennas that is used to compute the phase difference.

7.4   The Signal Processing Chain

The signal processing chain for MPGA is shown in figure 7.7. The first step of the algorithm takes range profiles of dimension (channels x azimuth pulses x range bins) as input, and extract the target to reduce the number of range bins for each azimuth pulses. The algorithm then compute the angle-of-arrival and phase differences of the extracted range profiles. the AOA has dimension of (1 x extracted range bins) per azimuth pulse, and the phase differences has dimension of (channels x channels x extracted range bins) per azimuth pulse. The third step was to compute c_{ij} and m_{ij} from the phase difference tensor and the AOA. And the last step was to compute the delta distances traveled in Azimuth, Range, and the change in heading.

7.5   Testing the Algorithm

7.5.1   Comparing between ideal track and computed track

The experiment setup used to test the MPGA is the same as in that in figure 7.3, where there are 4 custom corner reflectors scattered at arbitrary positions in the room, and the Radar being driven by a CNC motor for an aperture of 1 meter in side facing configuration.

The range profile of the received signal in channel 1 is presented in figure 7.8, where it can be observed there are 4 major trace of target over the aperture from range pixel 0 to 1000. Range beyond 1000 is behind the wall, and any reflectance in that region is the multi-path reflection of the signal. Those signal are not considered and is masked out in MPGA.
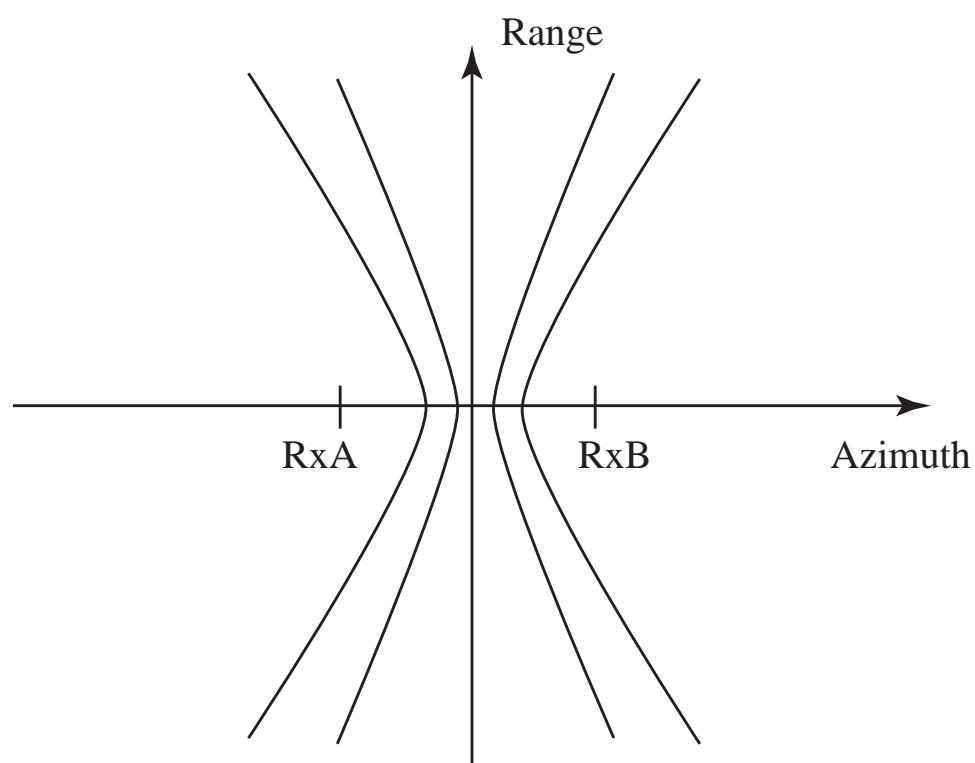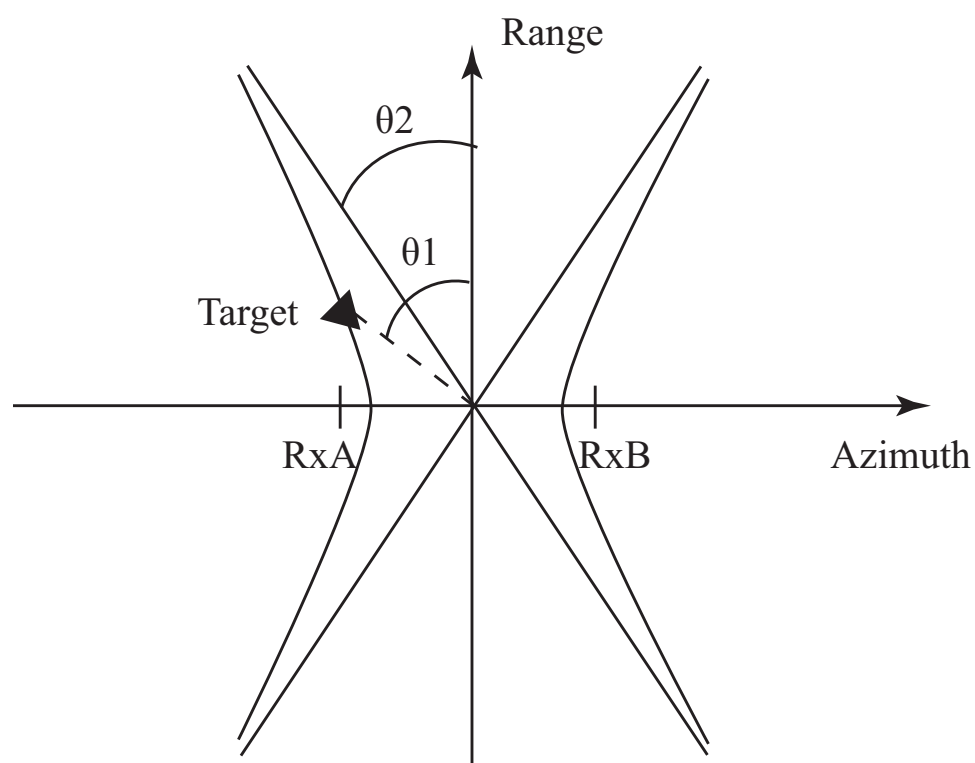
Figure 7.5. The estimated AOA

Figure 7.6. The mapping from estimated to true AOA
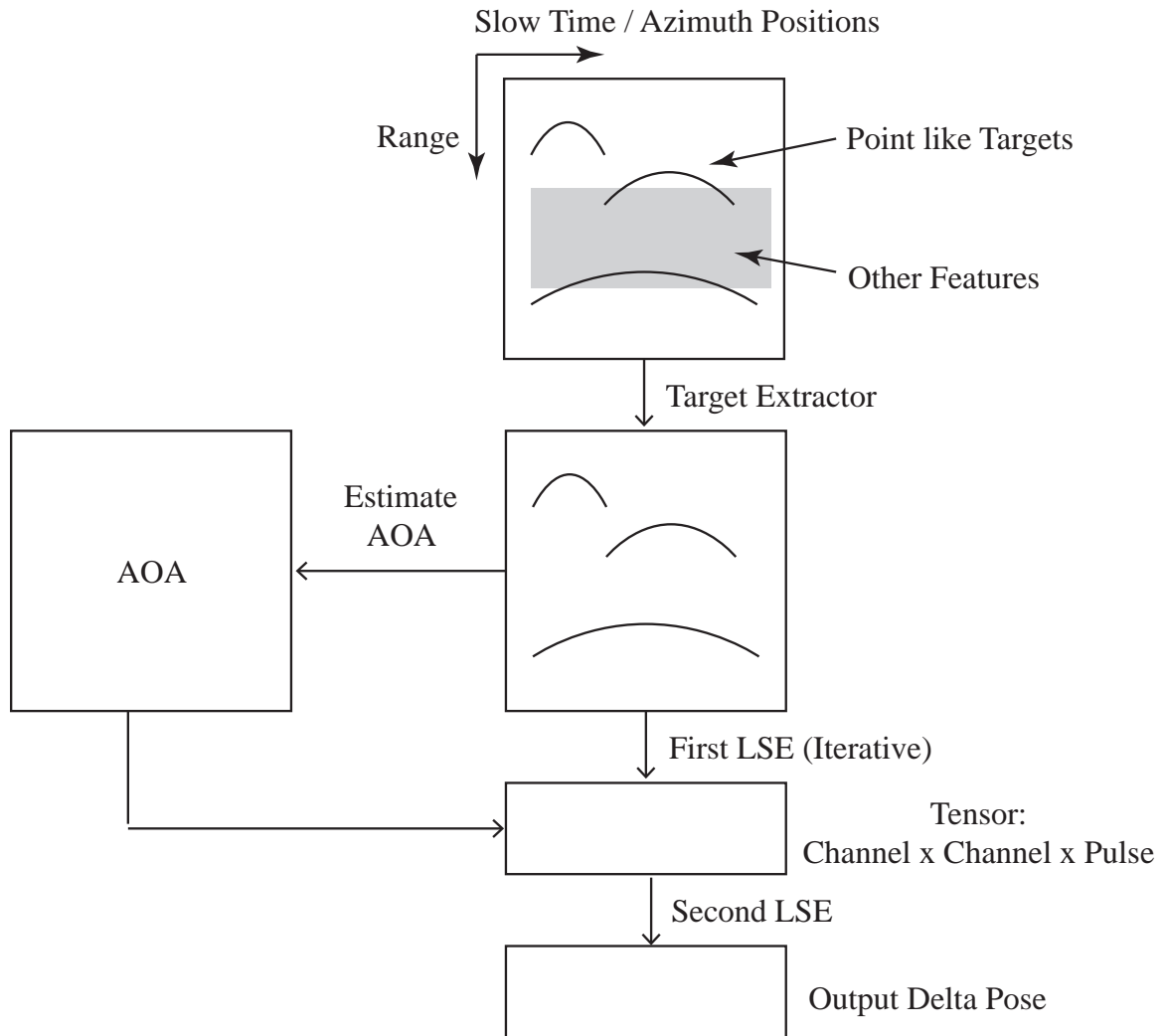
Figure 7.7. Signal Processing Chain of the MPGA

With multiple channels (2 channels was used in this example), the range profiles are inputted into the MPGA, and the track is computed in figure 7.9. Blue line represent the reference track recorded by the stepper motor, and red line represent the track computed by MPGA. Azimuth position is defined to be the azimuth axis of the radar antenna, which is parallel to the physical antenna baseline of the 2 channels, while range position is the axis perpendicular to the azimuth axis on the 2D imaging plane. It can be observed the computed track matched well with the reference track
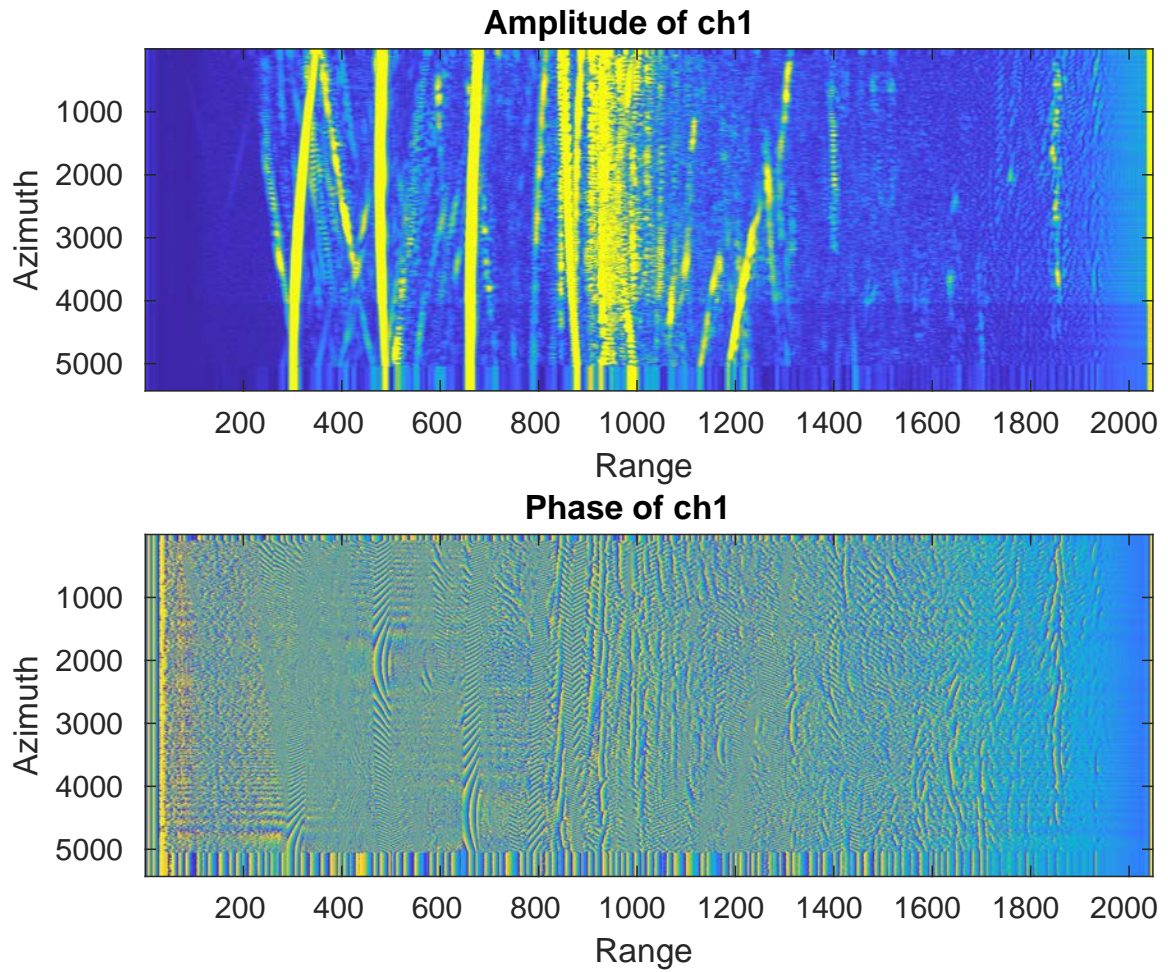
Figure 7.8. Range profiles of one channel in the MPGA test dataset

in azimuth position, the maximum discrepancy at the end of the track is about 2 millimeter. There is a significant discrepancy in the range position, where ideally the radar should not have any range direction motion. This discrepancy is caused by the squint of the radar antenna, such that the baseline of the antenna is not exactly aligned parallel with the direction of travel along azimuth, as a result, over the aperture it has estimated a range drift observed in the radar frame.
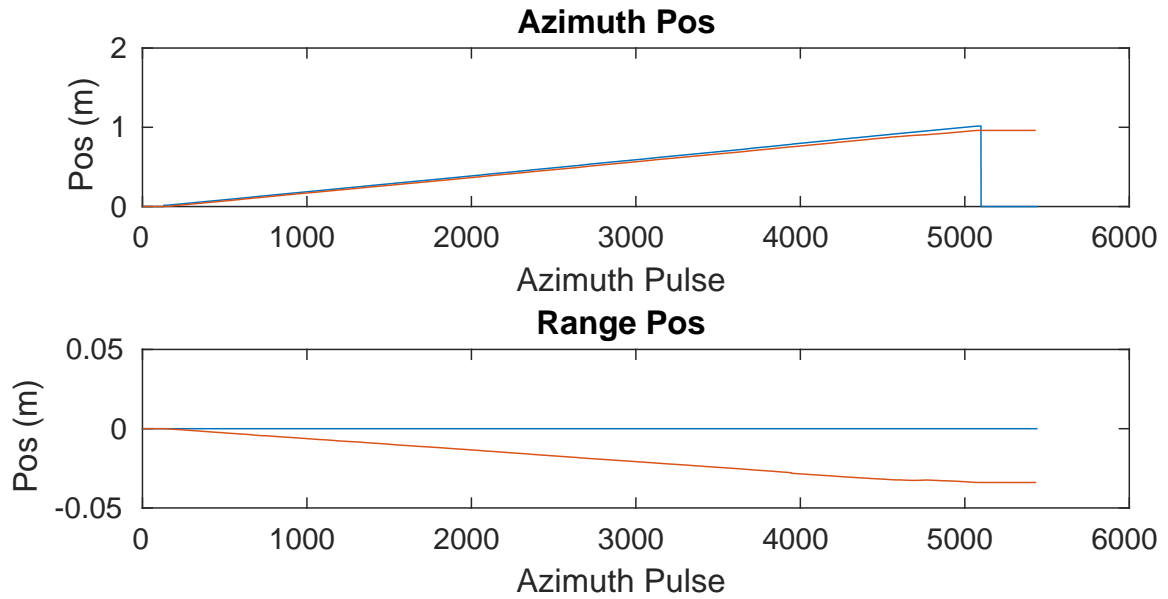
Figure 7.9. Reference track by the stepper motor (Blue) and track computed by MPGA (Red)

We compare the image focused using the ideal reference track recorded by the stepper motor (figure 7.10) versus the computed track using the MIMO return signal (figure 7.11). The signal compression was performed in time domain using the Fast Backprojection algorithm. It is expected the image formed by the reference track will be of optimal sharpness, and the computed track will be slightly off the optimal, but should still be retain most target features.
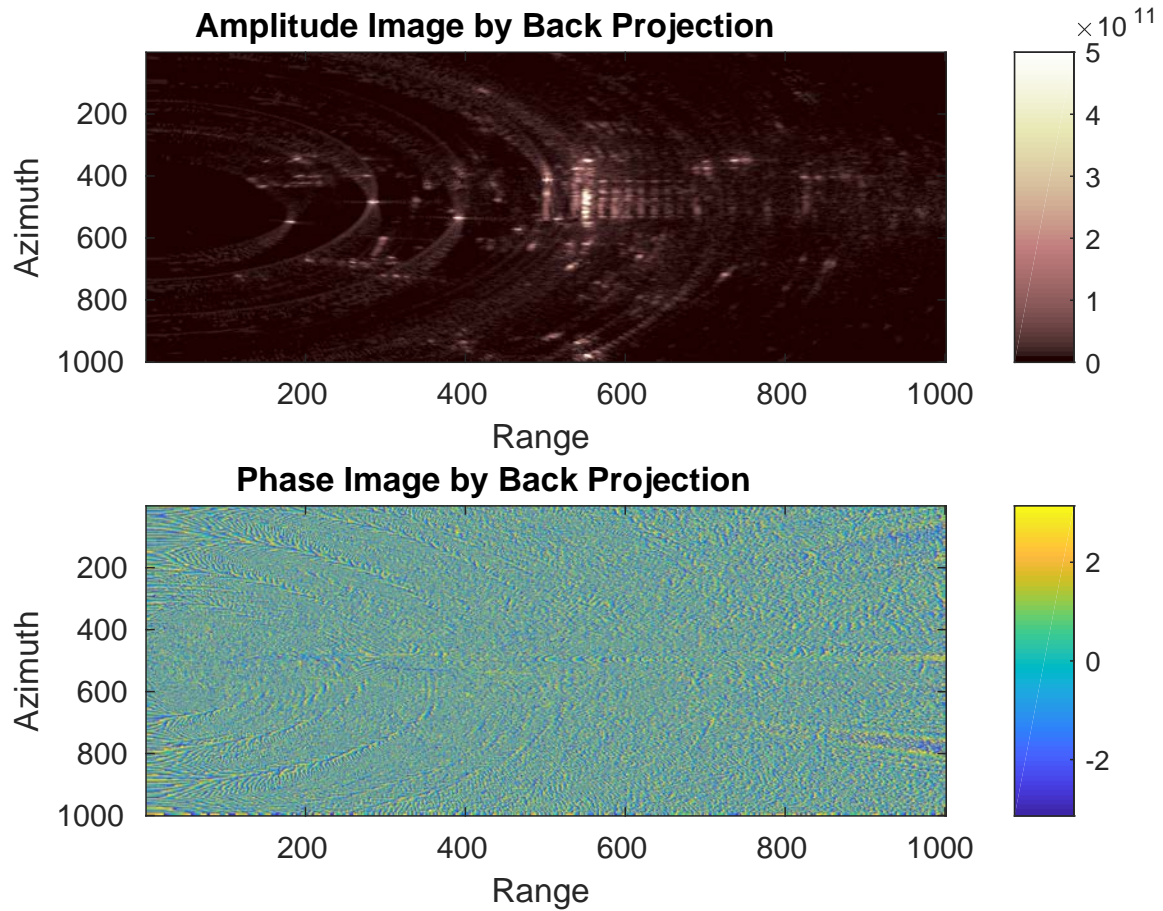
Figure 7.10. Backprojected image using reference track position

7.5.2 A deeper look into the accuracy of computing delta pose

It has been shown the computed track has attained very good result evaluated by comparing the sharpness of the focused image. To further justify the algorithm ability in calculating the radar platform motion, we look into the delta pose in 2 specific cases:

Radar sending chirp at irregular interval

We programmed the radar to transmit at a burst of a constant number of chirps, followed by a pause that has a duration of 3 chirps, then repeat. It is expected that between the chirps within the burst, the radar will be traveling at a constant
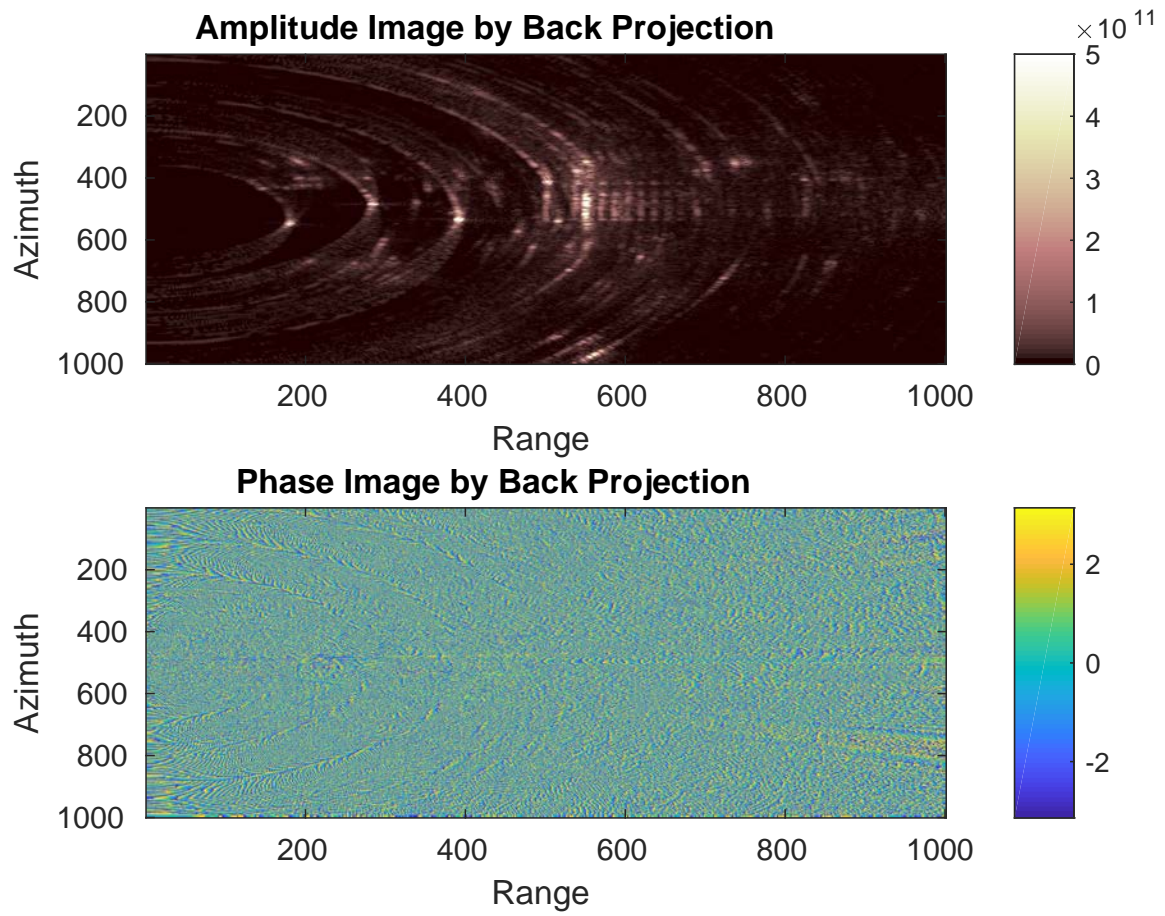
Figure 7.11. Backprojected image using MPGA

distance, while between bursts where there is a pause, the radar would have traveled for a longer distance. The result of the computed track is shown in figure 7.12.
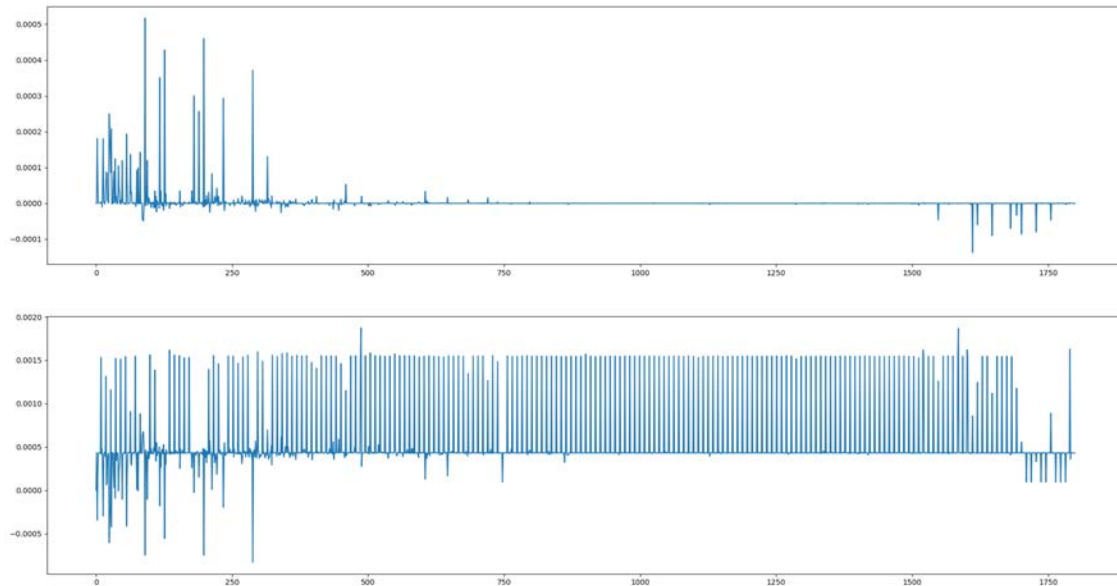
Figure 7.12. The computed δRange (upper) and δAzimuth (lower) for a chirp profile with burst followed by a pause of 3-chirps-duration

Observing the acceleration of the stepper motor

When the stepper motor starts moving, it has an acceleration which is not noticeable by just looking at it, however, measurable using the MPGA. We zoom in to the first few 2000 measurements of delta pose computed by MPGA, and observed the acceleration of the stepper motor.
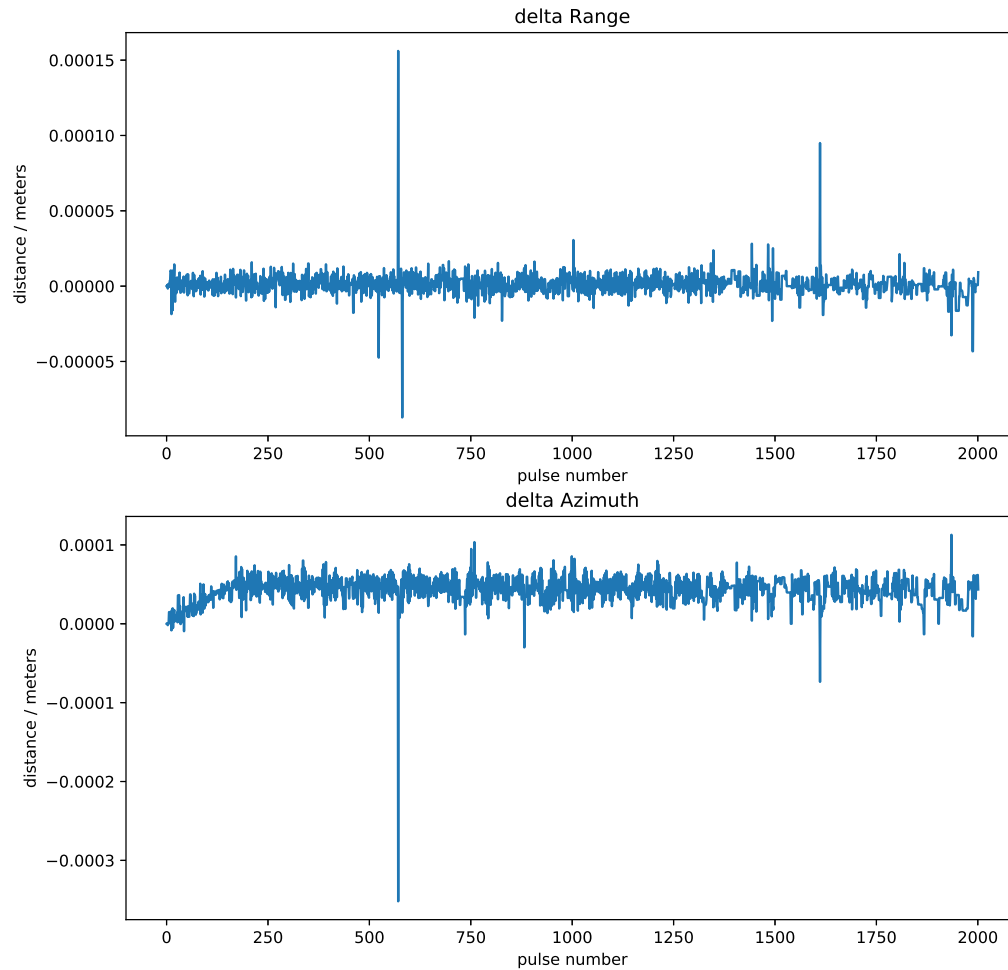
Figure 7.13. The computed δRange (upper) and δAzimuth (lower) for indicating the acceleration of the stepper motor

7.6 Advantages and Limitations

MPGA has some big advantages over conventional timing and positioning solution, because its measurement is "native" to the Radar antennas. For each pair of range profiles obtained from the antenna array, the change in radar pose is computed, there

is no need to interpolate the radar pose from another positioning sensor which has a different sampling rate and reference clock. As illustrated by the testing result, the measurement accuracy of MPGA was good enough to focus most of the target features in our test case. In addition, it was able to measure very short duration motion (e.g. the gap between burst of chirps) by its high updating rate, which might otherwise be missed by other positioning solutions.

The limitations of MPGA comes from the fact that it is using the return signal to compute the Radar pose, hence if there is nothing being illuminated by the Radar beam, the pose cannot be solved. In another word, the scene need to have some contrast. The assumption here is the scene is composed of targets which are uniformly distributed in angle-of-arrival for an unbiased estimation of the Radar pose.

Another limitation is the lack of absolute positioning capability. MPGA is more similar to INS than GNSS, in the sense that both INS and MPGA compute the pose by integrating the deltas, while GNSS compute the pose from an absolute global reference. Hence, MPGA is subject to drift.

To overcome these limitations, the author suggest a follow-up investigation on a sensor fusion solution which compose of MPGA, INS, and GNSS sensors for optimal positioning performance.

8. SUMMARY AND FOLLOWUPS

8.1 Achievements

We have demonstrated a SAR prototype mounted on a mobile platform operating a L-band. During the preliminary experiments, a transition was made to replace the PNA by SDR as a transceiver to lower the cost and improve the pulse repetition frequency. It was identified one biggest challenge in ground-based SAR system is the highly-nonlinear track that cause problem in focusing the SAR aperture. 2 novel algorithm was developed to aid with the SAR focusing problem when there is error in the track, the modified PGA, and the MIMO PGA. Modified PGA improves the sharpness of a pre-focused SAR image by analyzing the phase history along azimuth with the consideration of motion modeling. MIMO PGA provides an all-new timing and positioning solution that is capable of estimating the Radar pose using the MIMO range profiles. These algorithms are bundled with Backprojection (a time domain focusing method) and is proven to work with real data.

8.2 Future Plans

Existing SAR systems are mostly mounted on high-altitude aircraft or satellite, where the trajectory is very stable and locally linear over the synthetic aperture length. The cost of operating these systems are expensive, and the data availability and updating frequency has been an issue in many monitoring tasks. Overcoming the price burden and data availability requires operating the system on smaller and lower-altitude platforms, for example small UAVs. However smaller platforms and those closer to ground in general has less stable trajectory, sometimes it is even highly non-linear. Given the theoretical development and testing of the systems and algo-

rithms in this research, the author would like to extend the work to a UAV-mounted or ground vehicle-mounted SAR sensor solution that is capable of focusing the image under a highly non-linear trajectory. The availability of such SAR solution will eventually change the SAR community by allowing an easier deployment of systems, faster imagery updating interval, and at a previously impossible geometry.

REFERENCES

[1] A Ferretti, G Savio, R Barzaghi, A Borghi, S Musazzi, F Novali, C Prati, and F Rocca, "Submillimeter Accuracy of InSAR Time Series: Experimental Validation," IEEE Transactions on Geoscience and Remote Sensing, vol. 45, pp. 1142-1153, May. 2007.

[2] R Bamler, "A Comparison of Range-Doppler and Wavenumber Domain SAR Focusing Algorithms," IEEE Transactions on Geoscience and Remote Sensing, vol. 30, pp. 706-713, Jul. 1992.

[3] S Rodelsperger, A Meta. "MetaSensing's FastGBSAR: ground based radar for deformation monitoring" Proceedings of the SPIE, Volume 9243, id. 924318 8 pp. 2014

[4] O. Monserrat, M. Crosetto, G. Luzi. "A review of ground-based SAR interferometry for deformation measurement" ISPRS Journal of Photogrammetry and Remote Sensing. Volume 93, pp40-48. July 2014.

[5] Elachi, C. and J. van Zyl, "Introduction to the Physics and Techniques of Remote Sensing". John Wiley and Sons, 2006

[6] Curlander, J.C., McDonough, R.N. "Synthetic Aperture Radar: Systems and Signal Processing". Wiley, 1991.

[7] "Knowledge Base, Ettus Research" https://kb.ettus.com/Knowledge_Base Date: 10 April 2017

[8] "USRP Hardware Drive and Manual" https://files.ettus.com/manual/ Date: 10 April 2017

[9] M. Chim, D. Perissin, "Application of Ground Based Radar System in Structural Monitoring", Geoscience and Remote Sensing Symposium, 2016 IEEE International, Beijing, China, July 2016.

[10] M. Chim, D. Perissin, "Motion Compensation of L-band SAR using GNSS-INS", Geoscience and Remote Sensing Symposium, 2017 IEEE International, Texas, United States, July 2017.

[11] Byung-Lae Cho, Young-Kyun Kong, Hyung-Geun Park, and Young-Soo Kim, "Automobile-Based SAR/InSAR System for Ground Experiments" (2006) IEEE Geo- science and Remote Sensing Letters, Vol. 3, No. 3, July 2006, pp.401-405.

[12] D. Perissin, Z. Wang, H. Lin, "Shanghai subway tunnels and highways monitoring through Cosmo-SkyMed Persistent Scatterers", ISPRS Journal of Photogrammetry and Remote Sensing, 2012.

[13] O. Monserrat, M. Crosetto, G. Luzi, "A review of ground-based SAR interferometry for deformation measurement", ISPRS Journal of Photogrammetry and Remote Sensing, 2014.

[14] J. Hasch et al., "Millimeter-Wave Technology for Automotive Radar Sensors in the 77 GHz Frequency Band", IEEE Transaction on Microwave Theory and Techniques, 2012.

[15] Michael Schikorr. (2008). "High Range Resolution with digital stretch processing" Radar Conference, IEEE. Rome, Italy, 2008

[16] Bennet, John R. and Cumming, Ian G., "A Digital Processor for the Production of Seasat Synthetic Aperture Radar Imagery" (1979). LARS Symposia. Paper 316.

[17] Vincent Sarago, Mathieu Benoit, Yacine Bouroubi, Claire Gosselin and Michel Rheault, "Operational Use of SAR Interferometry for Surface and Infrastructures Movement Monitoring" (2014) IEEE Geoscience and Remote Sensing Symposium, 13-18 July 2014.

[18] Matus Bakona, Daniele Perissin, Milan Lazeckyc, Juraj Papcoa, "Infrastructure Non-Linear Deformation Monitoring Via Satellite Radar Interferometry" (2014) CENTERIS 2014 - Conference on ENTERprise Information Systems / ProjMAN 2014 - International Conference on Project MANagement / HCIST 2014 - International Conference on Health and Social Care Information Systems and Technologies.

[19] Armin W. Doerry, SAR Processing with Stepped Chirps and Phased Array Antennas, Sandia Report SAND2006-5855, Unlimited Release, September 2006.

[20] Michael Schikorr. (2008). "High Range Resolution with digital stretch processing" Radar Conference, IEEE. Rome, Italy, 2008

[21] Ian G, Cumming and Frank H. Wong (2005). Digital Processing of Synthetic Aperture Radar Data: Algorithms and Implementation., Artech House, ISBN: 978-1-58053-058-3.

[22] D. E. Wahl, P. H. Eichel, D. C. Ghiglia and C. V. Jakowatz, "Phase gradient autofocus-a robust tool for high resolution SAR phase correction", IEEE Transactions on Aerospace and Electronic Systems, vol. 30, no. 3, pp. 827-835, July 1994.

[23] Mulcahy-Stanislawczyk, John, "Properties of Ambiguity Functions" (2014).Open Access Theses. Paper 225.

[24] P. Samczynski and K. Kulpa, "Concept of the Coherent Autofocus Map-Drift Technique," 2006 International Radar Symposium, Krakow, 2006, pp. 1-4.

[25] H. Rohling, "Radar CFAR Thresholding in Clutter and Multiple Target Situations," in IEEE Transactions on Aerospace and Electronic Systems, vol. AES-19, no. 4, pp. 608-621, July 1983.

[26] S. Watts, "The performance of cell-averaging CFAR systems in sea clutter," Record of the IEEE 2000 International Radar Conference [Cat. No. 00CH37037], Alexandria, VA, USA, 2000, pp. 398-403.

[27] V Sarago, M Benoit, Y Bouroubi, C Gosselin and M Rheault, "Operational Use of SAR Interferometry for Surface and Infrastructures Movement Monitoring," IEEE Geoscience and Remote Sens- ing Symposium, 13-18 July 2014.

[28] P. H. Eichel and C. V. Jakowatz. "Phase-gradient algorithm as an optimal estimator of the phase derivative". Opt. Lett., 14(20):1101, 1989.

[29] W. L. Van Rossum, M. P. G. Otten, and R. J. P. Van Bree. "Extended PGA for range migration algorithms", IEEE Transactions on Aerospace and Electronic Systems, 42(2):478-488, April 2006

[30] Charles V. Jakowatz and Daniel E. Wahl. "Eigenvector method for maximum-likelihood estimation of phase errors in synthetic-aperture-radar imagery", J. Opt. Soc. Am. A, 10(12):2539-2546, 1993.

[31] Armin W. Doerry, E. Bishop Edward and A. Miller John. "Basics of Backprojection Algorithm for Processing Synthetic Aperture Radar Images". Sandia Report SAND2016-1682, Unlimited Release, February 2016.

[32] Mary J. Hicks, "On the Convergence of Phase Gradient Autofocus Algorithm for Synthetic Aperture Radar Imaging". Sandia Report SAND95-2364, Unlimited Release, January 1996.

[33] Armin W. Doerry, Volker Horndt, Douglas L. Bickel, and Richard M. Naething, "Estimating Radar Velocity using Direction of Arrival Measurements". Sandia Report SAND2014-17277, Unlimited Release, September 2014.

[34] Charles V. Jakowatz, Daniel E. Wahl, Paul H. Eichel, Dennis C. Ghiglia, and Paul A. Thompson. "Spotlight-Mode Synthetic Aperture Radar: A Signal Processing Approach". Norwell, MA: Kluwer Academic Publishers, 1996.

[35] K. S. Kulpa and J. Misiurewicz, "Stretch Processing for Long Integration Time Passive Covert Radar," 2006 CIE International Conference on Radar, Shanghai, 2006, pp. 1-4.

[36] William J. Caputi, Jr., Stretch: A Time-Transformation Technique, IEEE Transactions on Aerospace and Electronic Systems, Vol. AES-7, No. 2, pp269-278, March 1971.

[37] H. Schimpf, A. Wahlen, H. Essen, High range resolution by means of synthetic bandwidth generated by frequency-stepped chirps, IEE Electronics Letters, vol. 39, no. 18, pp 1346-8, 4 Sept. 2003.

[38] Z. Yunhua, W. Jie, L. Haibin, Two Simple and Efficient Approaches for Compressing Stepped Chirp Signals, Proceedings of the 2005 Asia-Pacific Microwave Conference APMC2005, Vols 1-5, pp 690-693, Suzhou, China, 4-7 Dec. 2005.

[39] D. C. Munson, Jr., "Computational Imaging," Ch . 17, Codes, Curves, and Signals: Common Threads in Communications, A. Vardy, Ed., Kluwer Academic Publishers, Boston, MA, 1998.

[40] Mohinder Jankiraman, "The Radar Ambiguity Function", Ch. 3, Design of Multi-Frequency CW Radars, Scitech Publishing Inc., Raleigh, NC, 2007.

A. USRP HARDWARE SPECIFICATIONS

The Antenna Specification

ELECTRICAL:

FREQUENCY:	(X.XX - X.XX) GHz - See Below Table for P/N
PATTERN:	DIRECTIONAL
POLARIZATION:	RHCP, LHCP, or LINEAR - See Below Table for P/N
ANTENNA GAIN :	15 dB
BEAM WIDTH:	EL: 40 Deg.
	AZ: 20 Deg.
VSWR:	2.0:1
OUTPUT IMPEDANCE:	50 ohms
POWER HANDLING:	100 watts
DC GROUNDING:	YES

LNA OPTION (For Rx Only):

LNA GAIN:	33 dB (P1dBout = +13 dBm)
LNA NOISE FIGURE:	2.2 dB
LNA VOLTAGE:	(+2.5 to +24) Volts DC
LNA DRAWING CURRENT:	< 30 mA

MECHANICAL:

SIZE:	9.39 in x 18.8 in x 0.56 in
WEIGHT:	1.35 lbs (612 g)
FINISH:	SKYDROL RESISTANT POLYURETHANE ENAMEL, AND BLACK ANODIZED
MATERIAL:	6061-T6 ALUMINUM ALLOY BASE COMPOSITE RADOME, IMPACT, ABRASION, UV, SOLVENT,AND SKYDROL RESISTANCE, FIRE RETARDANT
CONNECTOR:	TNC FEMALE (OPTION: SMA, QMA, SMB, N)

ENVIRONMENTAL:

TEMPERATURE:	-67 °F TO +185 °F [-55 °C TO +85 °C]
ALTITUDE:	30,000 ft.
VIBRATION:	> 20 G's
LEAKAGE:	HERMETICALLY SEALED

FEDERAL & MILITARY SPECIFICATIONS:

DESIGN TO:	FAA TSO-C144, DO-160D, D0-228, MIL-C-5541, MIL-E-5400, MIL-I-45208A, MIL-STD-810, AND SAE J1455

Figure A.1. Antenna Specifications

LNA Specification

Typical Test Results:

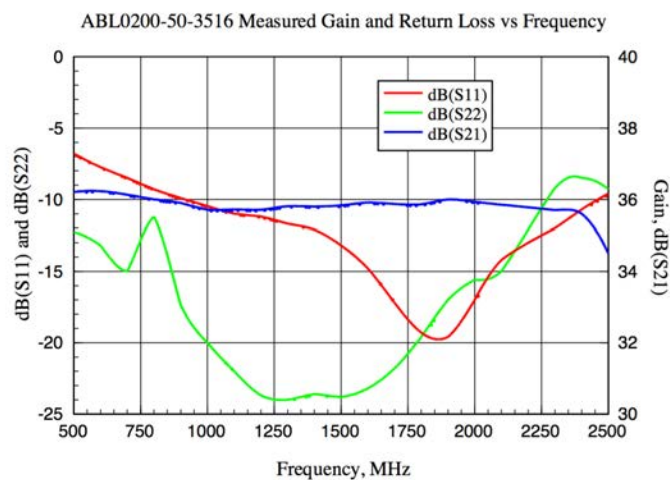Figure A.2. S11 S21 S22 of LNA ABL0200-50-3516

Electrical Specifications

Parameters	Minimum	Typical	Maximum
Frequency Range	1000 MHz		2000 MHz
Noise Figure @25°C		1.6dB	1.8dB
P-1dB Compression Point	+14dBm	+15dBm	
Nominal Gain @25°C	34 dB	35.5 dB	37 dB
Gain flatness		+/-0.25 dB	+/-0.5 dB
Gain Variation		+/-1.0dB	
Input VSWR		1.50:1	1.8:1
Output VSWR		1.35:1	1.5:1
Reverse Isolation		60dB	
Non Harmonic Spurious	-60 dBc		-60 dBc
Operating Temperature	-45°C		+85°C
Survival Temperature	-55°C		+125°C
DC Power Supply Voltage	+8 V	+12 V	+15 V
DC Power Supply Current	110 mA	120mA	130 mA
In/Out connectors	50 ohm SMA female		
Size	1.5"x0.85"x0.375		

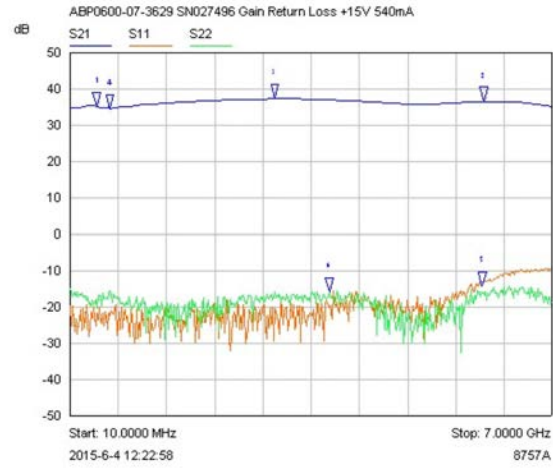Figure A.3. Specifications of LNA ABL0200-50-3516

PA Specification

Figure A.4. S11 S21 S22 of PA ABP0600-07-3629

Electrical Specifications

Parameters	Units	Specifications		
		Minimum	Typical	Maximum
Frequency Range	GHz	0.4		6.0
Small Signal Gain @25°C	dB	34.0	36.0	39.0
Noise Figure @25°C	dB		5.0	6.0
P-1dB Compression Point	dBm	+28.0	+29.0	
Output IP3	dBm	+35.0	+39.0	
Gain flatness	dB		+/-1.0	+/-1.5
Gain Variation over temp.	dB		+/-2.0	
Input VSWR			1.8:1	2.0:1
Output VSWR			2.0:1	2.5:1
Reverse Isolation	dB	45.0	50.0	
Non-Harmonic Spurious	dBc			-60.0
Operating Temperature	°C	-40		+75
Survival Temperature	°C	-55		+125
DC Voltage	V	+13.0	+15.0	+18.0
DC Supply Current	mA	480 mA	530 mA	650 mA
In/Out connectors		SMA Female		
Size	inches	1.5"x1.0"x0.4"		

Figure A.5. Specifications of PA ABP0600-07-3629

VITA

Man Chung Chim was born and grew up in Hong Kong. He has finished his Bachelor in Science (Physics) at the Chinese University of Hong Kong (CUHK) in 2013, and Master in Science (Physics) in 2014, during which he was a research assistant at the Institute of Space and Earth Information Science located in the CUHK campus, and the majority of research work was optical remote sensing. Chim started his PhD program at School of Civil Engineering, Purdue University, West Lafayette in January 2015, concurrent with Master in Electrical and Computer Engineering (ECE). He was granted with the Master in ECE in 2017. In October 2017, Chim has joined Zendar Inc., a startup company based in Berkeley, as a research engineer and is responsible for algorithm development used in focusing of dataset obtained from Synthetic Aperture Radars mounted on vehicles.